OPTIMIZING THE REFERENCE RADIUS FOR PREOPERATIVE SURGICAL PLANNING OF DISTAL RADIUS OSTEOTOMY

Stein van der Heide

9-5-2022

Head committee	*Prof. C. Brune*
Technological Supervisor	*J.M. Wolterink, PhD*
Medical supervisor	*A.J.H. Vochteloo, MD, PhD*
Process supervisor	*Drs. R.M. Krol*
External member	*Prof. Dr. Ir. G.J.M. Tuijthof*
Extra member	*F. De Graaff, PhD*

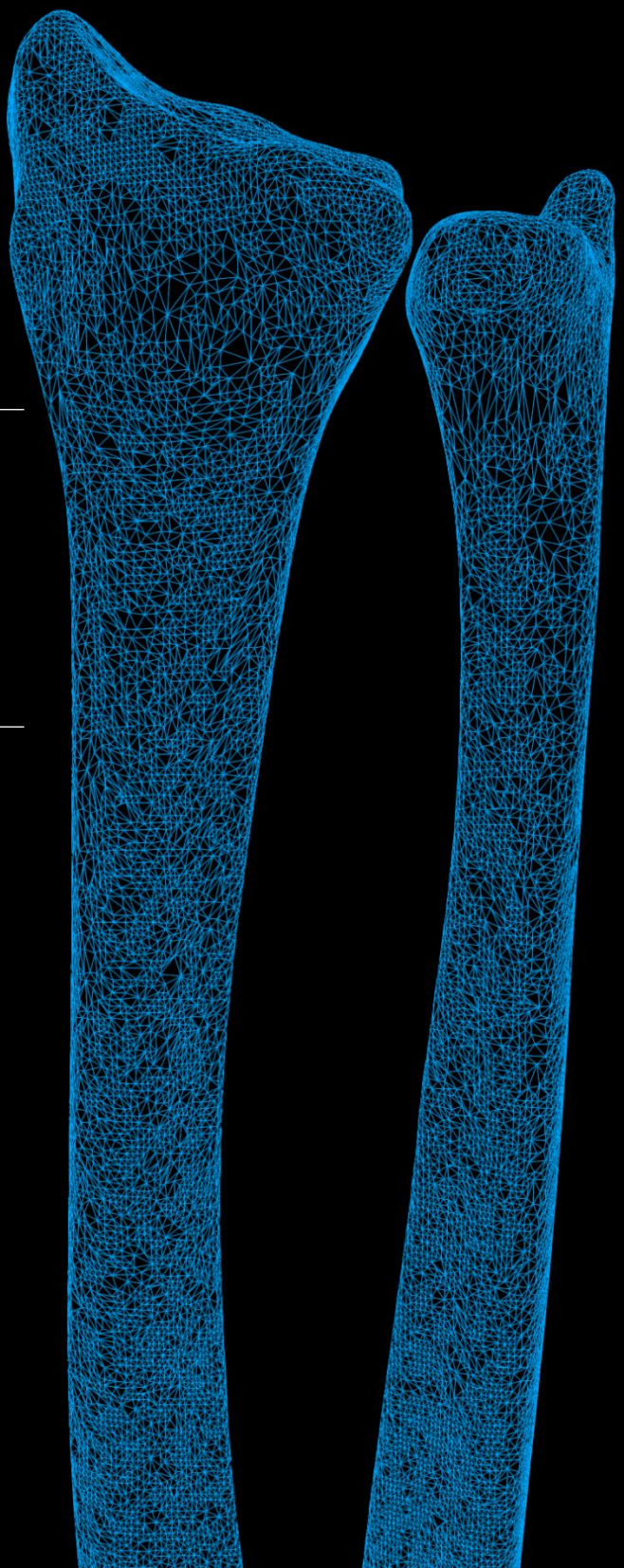

UNIVERSITY OF TWENTE.

OCON Orthopedische kliniek

Abstract

Introduction – Distal radius osteotomies for distal radius malunion can preoperatively be planned. Currently, the affected radius is compared with the contralateral unaffected radius to find what corrections are needed. However, problems arise if no healthy contralateral radius or asymmetry is present. Therefore, there is a need for an accurate reference radius. This thesis aims to describe the magnitude of asymmetry and offers an alternative reference radius in the form of a predicted radius.

Methods – Length asymmetry in the forearm was measured on 50 pairs of unaffected ulnae. Further, full shapes of radii were predicted given the shaft and proximal radius. This was done using a shape completion model based on Gaussian process regression. The model was trained on 57 healthy radii, and its performance was validated using a leave one out method. Differences between the predicted and original radius were expressed in mean and Hausdorff distances, rotational and translational differences, heatmaps of local differences, and as principal components of the differences. To assess how the model performs when a larger part of the radius is predicted, validation steps were repeated for 5%, 10% and a 15% predicted radius.

Results – An absolute left/right length difference in the ulna of 2.4 $\pm$ 2.3 mm was found. Further, the mean and Hausdorff distances between the 10% predicted radius and the original radius were 0.83 $\pm$ -0.24 mm and 3.11 $\pm$ 0.69 mm. The algorithm performed statistical significant better when 5% of the radius was predicted and worse if 15% was predicted. The rotational differences between the predicted and original distal radius around the x, y, and z-axis were: 0.19 $\pm$ 2.64 deg, 0.15 $\pm$ 2.49 deg, 0.07 $\pm$ 3.19 deg. Translational differences over the x, y, and z-axis were: 0.33 $\pm$ 4.74 mm, -0.23 $\pm$ 4.72 mm, and 0.31 $\pm$ 0.88 mm. Locally, differences were mainly present in the radial styloid.

Discussion – Significant left/right length asymmetry is present in the forearm, therefore, a length correction is needed when used for correction osteotomy. Further, when no contralateral radius is present, the shape of the distal radius can accurately be predicted. Because the shape of the radial styloid was predicted less accurately, it is advised to use other parts of the radius as a template for osteotomy. Lastly, an as large as possible part of the radius should be used to predict the radius.

Contents

Chapter 1

Introduction

Distal radius fractures are among the most prevalent fractures in the body with an incidence of 20-26 per 10. 000 person-years [1], [2]. Treatment most often consists of conservative therapy by using a cast or splint to stabilize the fracture. Additionally, in severe cases, surgical fixation can be used [3]. However, complications can occur in distal radius fractures [4]. One of the most prevalent complications is a malunion, contributing 17% to the total complications [5]–[9]. In malunion, bones are fused in an unfavorable orientation which does not restore the original shape. The distal radius can be rotated or shifted in all directions in respect to the pre-fracture situation. Clinically, radial tilt (rotation of the distal radius around the flexion/extension axis), radial inclination (rotation of the distal radius around the radial ab/adduction axis), and ulnar variance (a length difference in ulna and radius) can cause the majority of complaints (Figure 1). Complaints include pain, osteoarthritis, limitation of range of motion, and loss of grip strength [4], [10].

If a malunion is symptomatic, intervention might be required. Conservative therapy such as physiotherapy is the first choice, however, complaints may remain [6], [11]. In those cases, a corrective osteotomy can be considered. In a corrective osteotomy, the radius is sawn and then repositioned in a pose that should restore the original anatomical pose and is then fixated with a plate and screws [6], [10]. Previously, the saw plane and rations needed to reconstruct the radius were estimated preoperatively. To reconstruct the radius more precisely, 3D planned surgery can be used nowadays. In 3D planned surgery, a bilateral CT scan of the forearms is made. Then, a 3D representation of the CT scan of the contralateral radius is mirrored and superimposed on that of the malunited radius using 3D software. Thereafter, the proximal parts of both radii are aligned and the altered orientation of the distal malunited radius becomes visible. To correct this orientation, the distal radius is virtually sawn at the desired cut plane and rotated until it realigns with the unaffected radius. To execute this in practice, 3D printed patient-specific drill and saw guides (PSG) are used. The drill guide is used to predrill holes that match the holes in a volar plate if

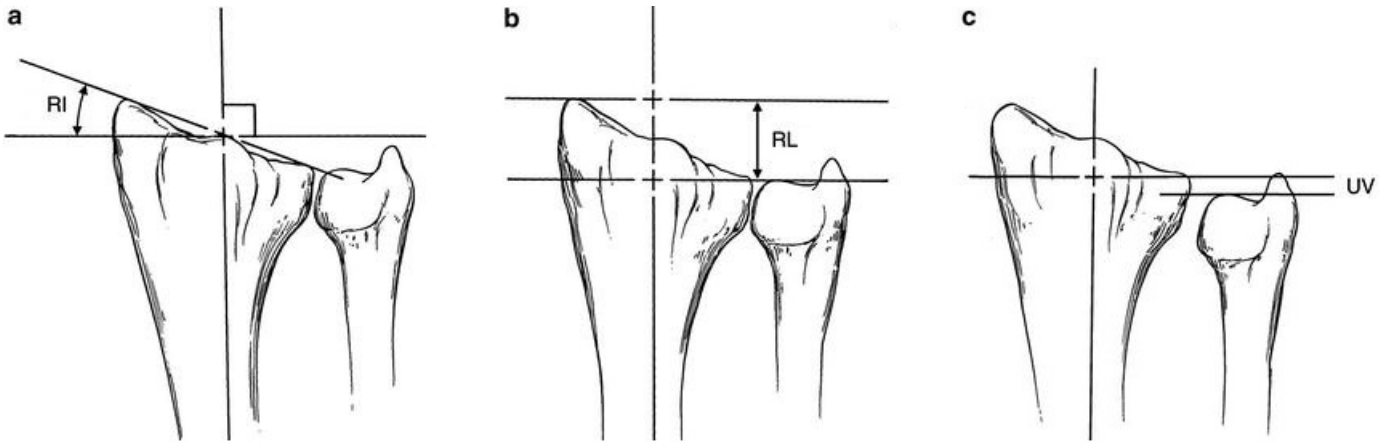

Figure 1.1: Radiological parameters for radius malunion. a) Radial tilt (rt), the angle in the direction of flexion/extension. b) Radial inclination (ri), the angle in the direction of radial/ulnar abduction. c) Ulnar variance (uv+), the length difference between radius and ulna. Adaptation from graham et al. (14)

the radius is rotated in the right orientation. The saw guide is used to locate the desired saw plane. This is visualized in Figure 2 [12]–[15]. When surgery is complete, the malunited radius should match the contralateral radius which is used as a reference radius. The challenge with planned surgery with PSG's is that an accurate reference radius is needed. If a reference radius does not mimic the pre-surgery radius, the restored radius will differ from the pre-fracture radius. Subsequently, the restored radius might still have an altered orientation and alignment. Clinically, this means that complaints may remain, and reintervention may be indicated. Therefore, there is a need for a reliable reference radius that can be used to restore the original anatomy.

The contralateral radius can be an accurate reference radius if good bilateral symmetry is present. Initially, some studies showed little bilateral difference by comparing X-ray images [16]–[19]. However, more recently, Vroemen et al. assessed symmetry by using CT scans [20]. They found that radii are more asymmetrical than initially thought. A relatively large right-left difference was found, especially in the length direction [20]. These bilateral asymmetries were found in a study that included 20 healthy subjects [20]. However, this study has limited power since only healthy subjects are included and bones can change shape depending on the mechanical load. To estimate the magnitude of asymmetry in the forearm more accurately asymmetry must be analyzed in a larger more relevant population. Therefore, we analyze the amount of bilateral asymmetry in the forearm in a larger population of patients with a distal radius malunion.

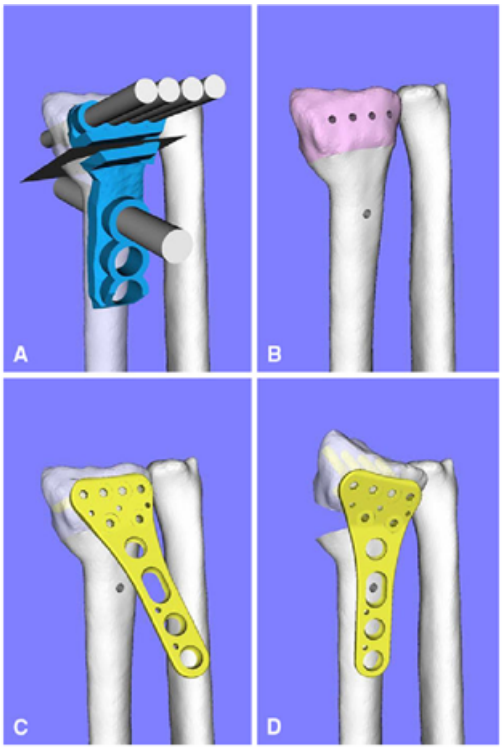

Figure 1.2: A 3-D computer simulation of a corrective osteotomy is shown. (a) Patient-specific saw and drill guides are made for osteotomies based on a contralateral reference radius. (b) The location of the cut plane and drill holes. (c) The plate is first fixated distally. (d) When the plate is also fixated proximally, the distal radius is repositioned to the planned position. From miyake et al.

In cases with large asymmetry in the contralateral radius, e.g., when a fracture or other pathology is present contralaterally, the contralateral radius cannot be used as a reference at all. To solve this problem, several attempts have been made to find an alternative reference radius using a statistical shape model and shape completion algorithms [21], [22]. These methods can predict the shape of the distal radius based on the shape of the proximal radius. These methods seem to work pretty well, however much is yet unclear about the performance of these algorithms. For example, Since the main goal of a correction osteotomy is to reconstruct congruent joints, the predicted reference radius must provide an accurate template for these areas. The local performances of the algorithms in these areas are not well described yet [21], [22]. Therefore, we created a shape completion algorithm that can predict the shape of the distal radius based on the shaft and the proximal radius and analyzed its performance.

The aim of this thesis is to further develop guided distal radius osteotomy by improving the understanding of the accuracy of the reference radius, for both the use of the contralateral radius and a predicted radius as reference bone. This will be done by measuring bilateral length symmetry, and developing an algorithm to predict a distal radius based on the shaft and proximal radius. Finally, the algorithm will be evaluated.

Chapter 2

Assessment of bilateral length asymmetry

2.1 Introduction

A distal radius malunion is a complication after a fracture in which the radius heals in a non-anatomical orientation [4]. Malunions can cause complaints including pain, loss of function, wrist instability, and, in the long term, osteoarthritis [4], [10]. This non-anatomical orientation of the distal radius is quantified with several radiological parameters: radial inclination, radial tilt, and ulnar variance (Figure 1) [10]. Complaints might especially exist when the ulna and radius are longitudinally misaligned in the distal radial ulnar joint (DRU) [23]. Therefore, ulnar variance is considered to be the most important parameter to explain complaints [20], [23]. Treatment often consists of conservative therapy1. If complaints remain after conservative therapy, a corrective osteotomy can be considered to restore the original anatomical relations in the DRU and radiocarpal joint [6], [11].

To allow for a precise reconstruction, three-dimensional (3D) planned and guided surgery is frequently used. The first step is to determine the location of the osteotomy, the required correction angles, and the translations needed to correct the radius to its original shape. This is done by mirroring a computed tomography (CT) derived 3D computer model of the affected radius. Then, this model is aligned with the unaffected radius. The difference in the pose of the distal radius in both forearms is then used to find the required saw-cut position, correction angles, and translations. Thereafter, a 3D printed guide is made which contains the required saw-cut position and drill holes to perform the preoperatively planned surgery. With this procedure, it is possible to reconstruct a malunited radius to mimic the shape of the contralateral unaffected radius [12], [14], [15], [24].

Problems with the use of the contralateral radius as a reference radius might arise in the case of bilateral asymmetry. If the contralateral radius does not represent the pre-fracture radius, the osteotomy will not restore the original anatomy of the radius [20], [21]. If the malunion is not corrected completely, complaints could persist, and re-intervention might be necessary. Since CT scans of healthy pre-fracture pairs of radii are not readily available, asymmetry must be quantified indirectly. Vroemen et al. found that the bilateral length difference of the ulna is correlated with the bilateral length difference of the radius by a factor of 0.984 [20]. Therefore, the length differences in the ulnae can be used to indicate the amount of forearm length asymmetry. This indirect way of measuring asymmetry in the forearm can only be used for length differences and not for differences in other translations and rotations that may be present. However, since ulnar variance is assumed to be the most important parameter to reconstruct in an osteotomy, a reference radius with an appropriate length is important [23]. Therefore, an indirect measurement of the forearm length differences is an important metric that can be used to assess the accuracy of the use of the contralateral radius as a reference radius.

In this chapter, we aim to quantify the bilateral ulnar asymmetry in a population of patients with a radius malunion. Studies suggest that mechanical-driven bone growth can cause bilateral differences [25]–[28]. Sex, workload, age, and other parameters can impact bilateral length differences [28]. Because a population of patients with a distal radius malunion may have other characteristics than a healthy population, a difference in bilateral length difference may also exist between populations. Therefore, it is important to understand how much bilateral asymmetry is present in a population of patients with a distal radius malunion.

2.2 Method

2.2.1 Patients and data

In this retrospective, descriptive, cross-sectional study, the bilateral length differences of 50 subjects were measured on forearm CT scans of patients who had an indication for a corrective osteotomy of the distal radius. All patients were treated at OCON Centre for Orthopedic Surgery in Hengelo, the Netherlands. Inclusion criteria were a bilateral CT scan of the whole forearm and age above 18 years. Exclusion criteria were a previous pathology in one of the forearms other than the distal radius malunion. Inclusion occurred in the period from February 2015 until June 2021.

CT- scan settings were based on a standard forearm scanning protocol and were

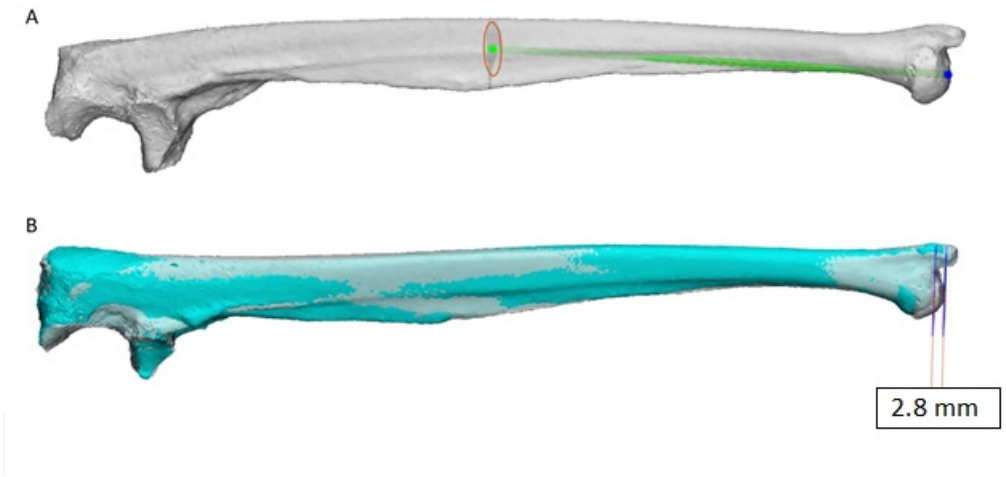

Figure 2.1: a) In green, the axis of measurement for bilateral ulnar length difference measurements is displayed. This axis is defined between the center of the ulna and the tip of the ulnar dome. The center of the ulna is defined as the center of a circle, fitted on the cross-section of an ulna which is cut lengthwise in half, b) a measurement for bilateral ulnar length differences. The left ulna (white) is mirrored and proximally aligned over the right ulna (cyan). In the direction of the previously determined measurement axis, the bilateral length difference is measured.

obtained before the corrective osteotomy. A slice thickness between 0.2 and 0.6 mm was used, with a B20 kernel and a matrix of 512x512. The voltage used was 120 kV and the tube current was automatically regulated. The forearms were placed in the scanning direction. Segmentation was done using the protocol in appendix A.

2.2.2 Measurements

The bilateral length differences were calculated by measuring the length difference between the aligned ulnae. The left ulnae were first mirrored and then aligned with the right ulnae by using a global rigid registration method and manual adjustment. Then, in the longest of the ulnae, a measurement axis was defined from the center of the ulnae to the top of the ulnar dome. The center of the ulna was found by cutting the ulna halfway between the most proximal part of the olecranon and the tip of the ulnar dome. Subsequently, a circle was fitted on the inner surface of the dissected bone. The axis of measurement was defined as an axis between the center of the fitted circle and the tip of the ulnar dome. This method is shown in Figure 2. The ulna length difference was then measured using this axis.

2.2.3 Statistical analyses

The required population size was estimated to be 65 using the following equation [29]:

$$N = \frac{Z^2_{\alpha/2} * std^2}{d^2} \tag{2.1}$$

Where N is the required population size,$Z_{\alpha/2}$ is the reliability coefficient, std is the expected standard deviation, and d is the desired one-sided width of the confidence interval. For a 5% two-tailed confidence interval, $Z_{\alpha/2}$ is 1.96. The standard deviation for bilateral radius length difference found in a previous study was 2.06 mm and was normally distributed [20]. We used the desired width of the confidence interval to be 0.5 mm on both sides.

To assess the reliability of our measurements, 19 measurements were repeated by a second-rater with experience in 3D measurements in forearm bones. Here, the mean inter-rater differences with standard deviation, and Intraclass Correlation Coefficient (ICC) were calculated. A Bland-Altman plot and correlation plot are also included.

The main outcome of this study was the mean and standard deviation of the absolute value of the bilateral length differences of the ulnae. Further, the relative mean and standard deviation were also calculated. In these relative measurements, patients were excluded if they were ambidextrous or if their dexterity was unknown because no dominant minus non-dominant calculation could be made. The results are visualized in violin plots. The analyses were done using Microsoft Excel (version 2022.)

2.3 Results

The general characteristics of the population are summarized in Table 1. The ulna on the dominant side was on average longer than the ulna on the non-dominant side, as can be seen in Figure 3a. The mean dominant minus non-dominant length difference was 0.8 ±3.2 mm. The absolute length difference has a folded normal distribution with a mean of 2.4 ±2.3 mm (figure 3b). The largest length difference was 7.7 mm. The mean difference between the observers was 0.0 ± 0.4 mm. The ICC was found to be 0.99, which is excellent. Figure 4 shows the measurements of both observers and a Bland Altman plot.

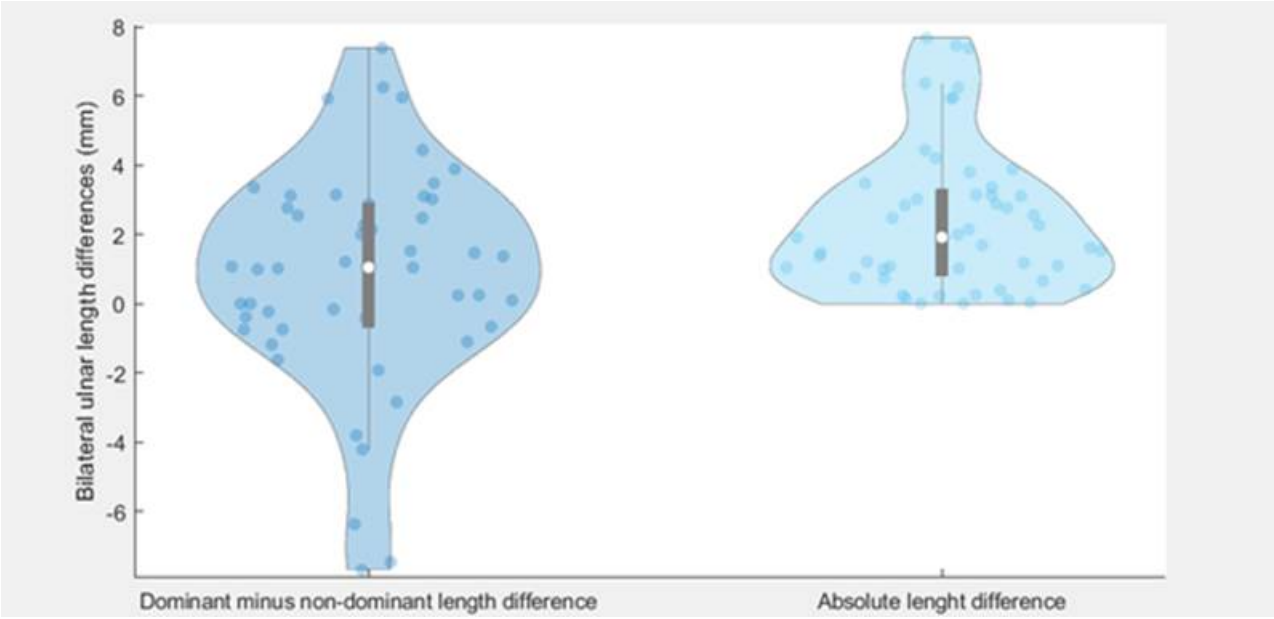

Figure 2.2: Violin plots of the bilateral ulnar length differences. A) The length difference between the dominant and non-dominant ulna. B) The absolute length difference between the dominant and non-dominant ulna. The width of the violin and the boxplot indicate the distribution of length differences.

Table 2.1: Characteristics of the population.

Sample size	N = 50
Age	
Mean	14 $\pm$ 18 Years
Sex	
Male	14 (27%)
Female	36 (73%)
Dexterity	
Right	41 (82%)
Left	7 (14%)
Unknown	1 (2%)
Ambidexterous	1 (2%)
Affected side	
Right	20 (40%)
Left	30 (60%

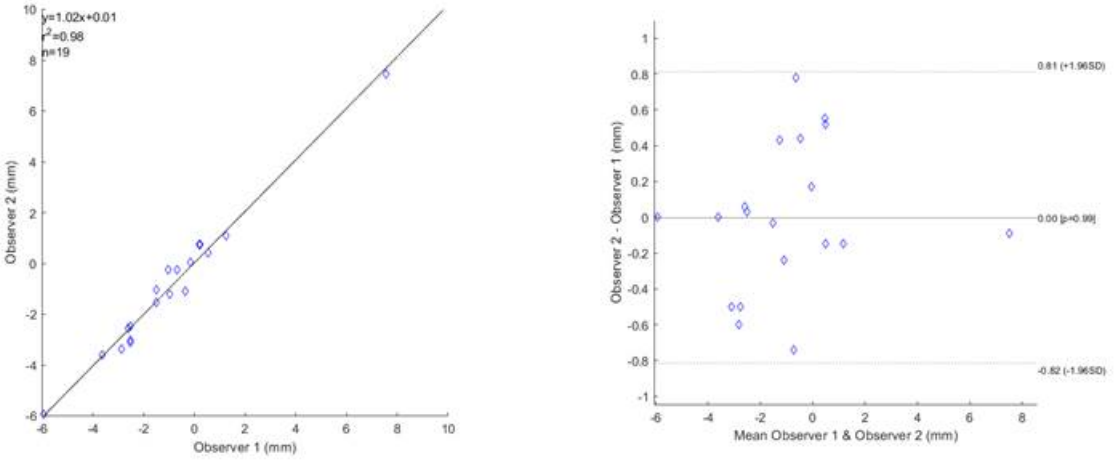

Figure 2.3: A) A correlation plot of the bilateral ulnar length measurements of observers 1 and 2. B) A Bland-Altman plot for the length measurements of observers 1 and 2.

2.4 Discussion

This study showed a substantial length difference within the bilateral pairs of ulnea in a population of patients with a distal radius malunion. On average, the difference was 2.4 mm and can be as large as 7.7 mm. Therefore, the application of the contralateral forearm as a template for corrective osteotomy can result in a large error if no correction is applied. This limits the use of the contralateral forearm without correction as a reference in guided distal radius corrective osteotomy.

Several previous studies found bilateral length differences in forearm bones, however, the extent of asymmetry in a relevant population is still unknown [20], [30]. Vroemen et al. found a strong right-side biased bilateral length difference of 2.08 mm (std: ±2.33mm) [20]. This difference was found in a population of 20 right-handed healthy subjects between an age between 22 and 56 years. Their results showed less asymmetry than ours and the dominant-sided was on average longer [20]. A recent paper from Hong et al. calculated asymmetry in a population of 132 subjects without forearm deformities with an average age of 61 years [30]. They showed a right-sided biased ulnar length difference of 1.85 mm and a difference of 1.46 mm in the length of the radii. However, they did not use absolute length differences which better indicates the amount of asymmetry [30]. The forearm length differences are hypothesized to be explained by mechanically driven bone growth and remodeling [25]–[28]. Because the left and right forearms receive a different mechanical load, length differences can exist, and therefore factors that influence mechanical

Figure 2.4: A) A strict application of the contralateral (cyan) forearm with proximal alignment as a template for the reconstruction of a malunited radius (white). The cyan forearm is longer as can be seen in the ulnar dome. B) The contralateral forearm is shifted until the heads of the ulnar dome align to compensate for the length difference. Now the distal ulna is aligned and the radius can be used as a template for a malunited radius.

load may influence bilateral length differences [25], [26]. Because a population of patients with a distal radius malunion is expected to have other characteristics than a healthy population, length differences might differ per population. Therefore, the differences between our study and previous research might partially be explained by the differences in population.

Our results show a larger bilateral ulnar length difference than previously thought. This difference translates to a similar length difference in the radius. When used as a template for osteotomy, this means that the reference radius can be longer or shorter than the affected radius. The ulnar variance of a healthy wrist is generally in the range of -1 to +2 mm. A larger ulnar variance is a predictor of complaints. Our results show that the contralateral radius can be longer or shorter than the affected radius by more than the normal ulnar variance. However, in practice, this problem can be solved with an approach similar to a technique suggested by Dobbe et al. [24]. In the design process for a surgical guide, the pairs of radius and ulna are aligned. If a length difference in the ulna is found, the healthy pair of radius and ulna are shifted to either distal or proximal until the distal ulnae align (Figure 5) [24]. Our data emphasize that the contralateral radius will be longer or shorter than the affected radius and a correction must be used.

The added value of our study is that we used a population of patients that had an indication for a distal radius osteotomy instead of a healthy population. The main disadvantage of the use of a population of patients with a distal radius malunion is that no healthy radii are available for symmetry assessment. However, Vroemen et al. showed a correlation of 0.98 between the bilateral length difference of the ulna and radius [20]. Therefore, the length difference of the ulna is considered to be a good indication of asymmetry of both bones of the forearm. Further, we did only investigate the length symmetry in the ulna and could not investigate other morphological parameters. However, the restoration of the ulnar variance is suggested to be one of the most important goals of a distal radius corrective osteotomy [23]. Therefore, the assessment of symmetry in the length direction is considered to be important.

Several sources of errors could be present in our measurements. At first, the slice thickness of the CT scan was up to 0.6 mm and segmentation errors could be present. Furthermore, errors might have been introduced in the measurement process. However, the methods used in our study had an excellent inter-observer variability with an ICC of 0.99, and the correlation plot and the Bland-Altman plot showed no inter-observer errors larger than 1 mm.

In conclusion, substantial forearm length differences are present in a population of patients with a radius malunion. This means that the contralateral forearm can only be used as a template for distal radius corrective osteotomy when a correction for length differences is applied [24]. Furthermore, alternative methods to estimate a reference radius might be explored, for example by using statistical shape models which predict the shape of a reference radius without using the contralateral radius [21], [22].

Chapter 3

The development of shape completion algorithm

3.1 Introduction

Patient-specific surgical guides increases in popularity in orthopedics [31] To surgically correct a certain bony deformation, the bone is sawed, subsequently rotated and translated, and eventually fixated with a plate and screws. Usually, the rotations and translation needed for reconstruction are found before surgery by comparing the 3D computer model of the bone of the affected side with the model of the healthy contralateral side. However, if both sides are fractured, no comparison can be made [31]. One example of this is in distal radius corrective osteotomy [12], [13]. Here a radius bone heals in an anatomical orientation after a fracture. Because this is one of the most common fractures, a contralateral previous fracture is not uncommon [1], [2]. This problem may be overcome with the use of a shape completion algorithm6. In this algorithm, the shape of the distal radius is computed with a given proximal radius as input. By doing so, no contralateral radius is needed and patient-specific guides can also be made for patients without no healthy contralateral bone available. For further validation of shape completion algorithms, an algorithm must be made. Therefore, this chapter aims to describe a method to predict the shape of the distal radius.

Two previous attempts have been made to predict the shape of the distal radius using statistical shape models (SSM). Oura et al. used partial least squares regression [22], whereas Mauler et all used Gaussian process regression [21]. Both methods of regression were able to predict the distal radius. However, Mauler et al achieved better results using Gaussian process regression [21]. Furthermore, unlike the method of Oura, the method of Mauler et al. was well documented. This makes Gaussian process regression a viable choice to create a shape

An added benefit of working with these SSMs is that they provide us with a visual representation of the shape variation [32]. Often, variation in shapes is only expressed as a clinical parameter in orthopedics. However, this often only covers one aspect of the shape and ignores everything else. The principal components of the shape variation can display the major ways the shapes vary in our dataset [32]. This may help orthopedic surgeons to better understand the shapes of the radius.

In this chapter, we describe a mathematical framework for a Gaussian process regression shape completion model and how it can be applied to a dataset with radius bones. Further, the shape variation of the radius is visualized.

3.2 Method

3.2.1 Patients and data

To create a statistical shape model, we included 57 CT scans of healthy radii. The healthy radii were obtained from subjects that were suspected of a distal radius malunion and therefore underwent a CT scan of the affected and unaffected contralateral radius. Inclusion criteria were a bilateral CT scan of the whole forearm and age of $>$18 years. Exclusion criteria were a previous pathology in one of the radii other than the malunion. Inclusion occurred between February 2015 and June 2021.

CT- scan settings were based on a standard forearm scanning protocol and were obtained before the corrective osteotomy. A slice thickness between 0.2 and 0.6 mm was used, with a B20 kernel and a matrix of 512x512. The voltage used was 120 kV and the tube current was automatically regulated. The forearms were placed in the scanning direction. Segmentation was done using the protocol in appendix A.

3.2.2 Preprocessing

Before the CT scans could be incorporated into the SSM, a few preprocessing steps were done. Then 3D surface models were subsequently made for all radii using the Mimics software (Materialize, Leuven, Belgium) After that, the shapes were aligned in 3D space. The shapes were manually translated and rotated the shapes to align with the reference shape. This alignment was done to align the radii proximally as close as possible. Lastly, before the radii can be incorporated into the SSM, correspondence between shapes must be established. This means that we must know for all points on a shape, what points correspond with that point on another

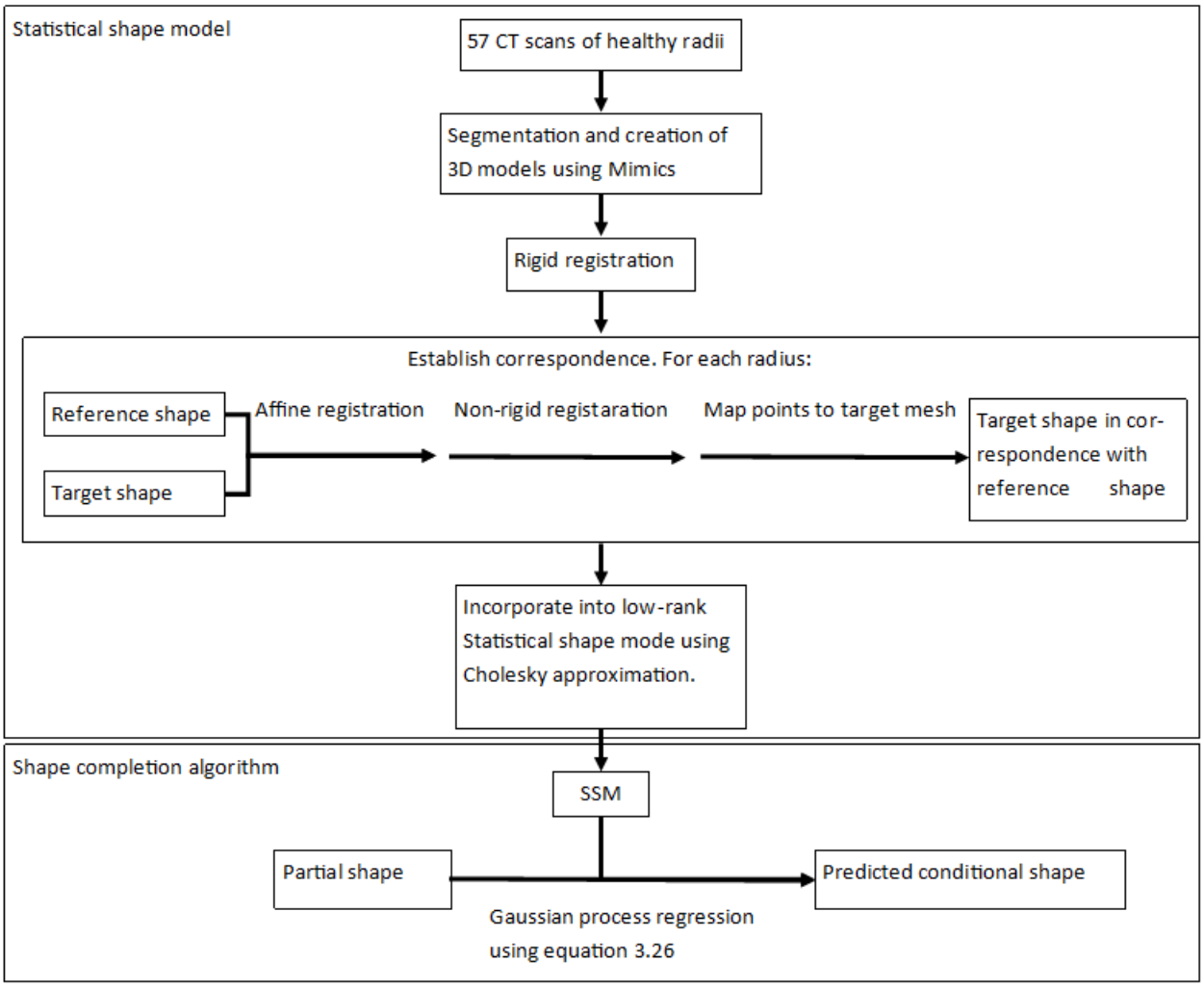

Figure 3.1: A schematic visualization of the creation of the statistical shape model and the shape completion algorithm. The first part shows the preprocessing steps, the establishment of correspondence and the creation of the statistical shape model (SSM). The second part shows how the statistical shape mode can be used to predict a conditional shape based on a partial shape.

shape. This correspondence was established using a rigid and non-rigid registration. This non-rigid registration was based on Gaussian processes. To explain the non-rigid registration and the GPMM, first, we have to explain Gaussian processes.

3.2.3 Description of shapes

In statistical shape modeling, shapes are often described as a linear combination of deformation vectors. The first step to doing this, is to represent the bone as a finite collection of points in 3D space. The set of points Γ_R that describes a reference *R* shape can be denoted as:

$$\Gamma_R = \left\{ x \mid x \in R^3 \right\} \tag{3.1}$$

Where *x* are the 3D coordinates of the points. Different shapes can then be expressed as a deformation field between each point on a reference shape and a corresponding point on a shape we are interested in. The 3D deformation vector field *u* is expressed as:

$$u : \Gamma_R \to R^3 \tag{3.2}$$

Where each point in Γ_R is mapped to a corresponding point on a shape we are interested in. Any shape can now be expressed as a deformation vector field from a reference shape. A condition to do this is that shapes must be in correspondence.

3.2.4 Gaussian process

The variation in shapes in a dataset can be expressed as a mean function and a covariance function. The mean and a covariance express for each point i on the reference shape Γ_R what the mean deformation vector $u(i)$ is for that point over a dataset and describe the covariance of all vectors $u(i)$ in our dataset.

To explain what the covariance function is, we first need to understand what a univariate normal distribution is. This describes the distribution P of a random variable x that is normally distributed around a mean μ with variance σ^2:

$$p(x) = N\left(\mu, \sigma^2\right) \tag{3.3}$$

The mean describes the location of the function, and the variance describes how spread out the data is. A multivariate normal distribution expresses how two or more variables are jointly distributed:

$$p\left(x_1, x_2\right) = N\left(\begin{pmatrix} \mu_1 \\ \mu_2 \end{pmatrix}, \begin{pmatrix} \sigma_1^2 & \sigma_{12} \\ \sigma_{12} & \sigma_2^2 \end{pmatrix}\right) \tag{3.4}$$

In this two-dimensional case, the distribution of variables x_1 and x_2 is defined. The location of the distribution defined with the mean functions μ_1 and μ_2. The variance σ_1^2 and σ_2^2 determine how spread out the probability is along each dimension. The covariance σ_{12} shows how x_1 and x_2 can change together and is therefore a measure of the correlation between x_1 and x_2. Note that the covariance between x_1 and x_2 is the same as the covariance between $x_2$and x_1. In a simple example of hand width and hand length, μ_1 and μ_2 stand for the mean hand length and hand width, respectively, whereas σ_1^2 and σ_2^2 correspond to the variance in these measures. Covariance σ_{12} is a measure of the correlation between x_1 and x_2 and expresses how the length and width vary together.

To model shapes, the multivariate normal distributions can be applied on the deformation field of a given set of shapes. The deformation vector $u(i)$ exists of an x, y and z component:

$$u(i) = \begin{pmatrix} u_x(i) \\ u_y(i) \\ u_z(i) \end{pmatrix} \tag{3.5}$$

For each point i on the template surface, we can model the distribution of its 3D deformation vector as a multivariate normal distribution. The probability for the 3D location point i is:

$$P(u(i)) = N\left(\begin{pmatrix} \bar{u}_x(i) \\ \bar{u}_y(i) \\ \bar{u}_z(i) \end{pmatrix}, \begin{pmatrix} \Sigma_{xx}(i) & \Sigma_{xy}(i) & \Sigma_{xz}(i) \\ \Sigma_{yx}(i) & \Sigma_{yy}(i) & \Sigma_{yz}(i) \\ \Sigma_{zx}(i) & \Sigma_{zy}(i) & \Sigma_{zz}(i) \end{pmatrix}\right) \tag{3.6}$$

$\mu(i)$ is the mean for each x- y- and z-coordinate and is called the mean vector:

$$\mu(i) = \begin{pmatrix} \bar{u}_x(i) \\ \bar{u}_y(i) \\ \bar{u}_z(i) \end{pmatrix} \tag{3.7}$$

$k(i)$ expresses the covariance between the x- y- and z-coordinates and is called the covariance matrix.

$$\mathrm{k}(i) = \begin{pmatrix} \Sigma_{xx}(i) & \Sigma_{xy}(i) & \Sigma_{xz}(i) \\ \Sigma_{yx}(i) & \Sigma_{yy}(i) & \Sigma_{yz}(i) \\ \Sigma_{zx}(i) & \Sigma_{zy}(i) & \Sigma_{zz}(i) \end{pmatrix} \tag{3.8}$$

We can already see the probabilistic properties of a model because we can already describe the distribution of a single point in 3D space. The model becomes more interesting when it is extended to multiple points. For example, for a shape

consisting of two points, deformation vectors $u(i_1)$ and $u(i_2)$can be jointly described as:

$$\begin{pmatrix} u\left(i_1\right) \\ u\left(i_2\right) \end{pmatrix} = \begin{pmatrix} u_x\left(i_1\right) \\ u_y\left(i_1\right) \\ u_z\left(i_1\right) \\ u_x\left(i_2\right) \\ u_y\left(i_2\right) \\ u_z\left(i_2\right) \end{pmatrix} \tag{3.9}$$

The probability distribution can then be described as:

$$P\begin{pmatrix} u\left(i_1\right) \\ u\left(i_2\right) \end{pmatrix} =$$

$$N\left(\begin{pmatrix} \bar{u}_x\left(i_1\right) \\ \bar{u}_y\left(i_1\right) \\ \bar{u}_z\left(i_1\right) \\ \bar{u}_x\left(i_2\right) \\ \bar{u}_y\left(i_2\right) \\ \bar{u}_z\left(i_2\right) \end{pmatrix}, \begin{pmatrix} \Sigma_{xx}\left(i_1,i_1\right) & \Sigma_{xy}\left(i_1,i_1\right) & \Sigma_{xz}\left(i_1,i_1\right) & \Sigma_{xx}\left(i_1,i_2\right) & \Sigma_{xy}\left(i_1,i_2\right) & \Sigma_{xz}\left(i_1,i_2\right) \\ \Sigma_{yx}\left(i_1,i_1\right) & \Sigma_{yy}\left(i_1,i_1\right) & \Sigma_{yz}\left(i_1,i_1\right) & \Sigma_{yx}\left(i_1,i_2\right) & \Sigma_{yy}\left(i_1,i_2\right) & \Sigma_{yz}\left(i_1,i_2\right) \\ \Sigma_{zx}\left(i_1,i_1\right) & \Sigma_{zy}\left(i_1,i_1\right) & \Sigma_{zz}\left(i_1,i_1\right) & \Sigma_{zx}\left(i_1,i_2\right) & \Sigma_{zy}\left(i_1,i_2\right) & \Sigma_{zz}\left(i_1,i_2\right) \\ \Sigma_{xx}\left(i_2,i_1\right) & \Sigma_{xy}\left(i_2,i_1\right) & \Sigma_{xz}\left(i_2,i_1\right) & \Sigma_{xx}\left(i_2,i_2\right) & \Sigma_{xy}\left(i_2,i_2\right) & \Sigma_{xz}\left(i_2,i_2\right) \\ \Sigma_{yx}\left(i_2,i_1\right) & \Sigma_{yy}\left(i_2,i_1\right) & \Sigma_{yz}\left(i_2,i_1\right) & \Sigma_{yx}\left(i_2,i_2\right) & \Sigma_{yy}\left(i_2,i_2\right) & \Sigma_{yz}\left(i_2,i_2\right) \\ \Sigma_{zx}\left(i_2,i_1\right) & \Sigma_{zy}\left(i_2,i_1\right) & \Sigma_{zz}\left(i_2,i_1\right) & \Sigma_{zx}\left(i_2,i_2\right) & \Sigma_{zy}\left(i_2,i_2\right) & \Sigma_{zz}\left(i_2,i_2\right) \end{pmatrix}\right) \tag{3.10}$$

With these equations, we jointly described two points on the surface. As one can see, the mean coordinates of both points are expressed as a mean vector in the first part of the normal distribution. The second part of the joint normal distribution consists of four blocks. Block (1,1) in blue describes the covariance matrix of the x, y, and z coordinates of the point i_1 as earlier described. Block (2,2) in orange does the same for point i_2. Blocks (1,2) and (2,1) describe the covariance matrix for all x y and z coordinates between points i_1 and i_2. With this joint covariance matrix, we can describe the prediction of the 3D location of the dependent points i_1 and i_2.

The example above for two points can be generalized for an infinite number of points. To generalize these vectors and matrices to infinite dimensions, a mean function and a covariance function can be used. However, thanks to the marginalization property of the Gaussian process, the math also works for finite-dimensional matrices instead of functions. When represented as functions, define, for an infinite set of points on shape γ_R, a mean function $\vec{\mu}$ and a covariance function K are defined, where:

$$\vec{\mu} = (\mu(i))_{i \in \Gamma_R} \tag{3.11}$$

And:

$$K = \left(k\left(i_a, i_b\right)\right)_{i_a, i_b \in \Gamma_R} \tag{3.12}$$

Together, a multivariate normal distribution can be formed over these functions:

$$P(u) = N(\vec{\mu}, K) \tag{3.13}$$

When discretized, this results in a mean vector and a large covariance matrix. This multivariate normal distribution encodes the mean deformations in a dataset, the variation of each x, y, and z coordinate for each deformation, and correlations between all x, y, and z coordinates of all points. This is also known as a discretized version of a Gaussian process. Conversely, the Gaussian process is the continuous representation of the discretized multivariate normal distribution.

Because the discrete multivariate normal distribution contains the joint probability of all points of a shape, it provides information about the probability of shapes. For example, this can tell what shapes are probable to happen, and therefore if it is pathological or not. Furthermore, we can calculate confidence regions of shapes that are probable to exist

3.2.5 Low rank of Gaussian processes

A problem with working with discrete Gaussian processes is their computational challenges. 3D computer models of bones of the radius usually have around 25,000 points. The size of the covariance matrix is (3* the number of points) x (3* the number of points). This means that the covariance matrix can easily consist of more than 5.6 billion points, which cannot be feasibly stored in a computer's memory.

To compress the multivariate normal distribution to a lower dimensionality, principal component analysis can be performed. This is done using a Karhunen - Loève expansion. By doing so, the multivariate normal distribution $N(\vec{\mu}, K)$, is expressed as a mean deformation $\vec{\mu}$, and the principal components $\alpha\sqrt{\lambda}\phi$ of the covariance matrix such that:

$$N(\vec{\mu}, K) = \vec{\mu} + \alpha_1\sqrt{\lambda_1}\phi_1 + \alpha_2\sqrt{\lambda_2}\phi_2 + \alpha_3\sqrt{\lambda_3}\phi_3 + \dots \tag{3.14}$$

ϕ_i are the eigenfunctions and λ_i are the associated eigenvalues. These can be thought of as vector fields that explain variation. $\sqrt{\lambda_1}\phi_1$ is chosen so that this vector field explains most of the variation in the covariance matrix. $\sqrt{\lambda_2}\phi_2$ is chosen so that it explains most of the variation that is left and so on. More general:

$$N(\vec{\mu}, K) = \vec{\mu} + UD\alpha = \vec{\mu} + Q\alpha \tag{3.15}$$

Where U includes all eigenfunctions, D all eigenvalues, and Q contains the principal components of the shape variation of a dataset. ($Q = UD$). By varyingα for

each component, we can create new shapes that follow the distribution of the shapes used to define the model, given a covariance matrix. If infinitely many principal components are available, this method can cover all information from the covariance matrix [33]:

$$K = UD^2U^T \tag{3.16}$$

However, in practice, a low-rank approximation is always used because for computational ends, a finite number of principal components is needed. This is called the prior model.

As described can any covariance matrix now be expressed with a finite number of principal components. However, U and given D must still be estimated from the covariance matrix. This can be done using a Pivoted Cholesky approximation. Now we can express the covariance of all points of a dataset op shapes as a convenient low-rank prior model.

3.2.6 Correspondence

To be incorporated in the SSM, the 3D computer models must be in correspondence. This means that we have to know which point on a reference shape, matches with which point on another shape belongs to that point. This correspondence was established by mapping all the points of a reference shape (the moving shape) to the surface of any other shape(the target shapes). First, an affine landmark registration was done in which the moving shape was translated, rotated, and scaled to match the landmarks on the target shape as well as possible using Procrustes analysis. The landmarks used were the center of the radial head, the tip of the radial styloid, and the center of the ulnar notch. Once the moving shape is rigidly aligned with the target shape, non-rigid registration is done using a Gaussian process.

In this method, a Gaussian process was formed with functions instead of data. A Gaussian process was formed with as mean the rigidly aligned reference radius. Besides, a diagonal kernel was used with a variation of σ = 13 mm. This means that the Gaussian process could model shape variations around the reference shape, with the constraint that points in 3D space are correlated with neighboring points with a Gaussian distribution with a standard deviation σ of 13 mm. A low-rank approximation of this Gaussian process was done with a Cholesky approximation. The principal components are then optimized to match the reference shape to the target shape as well as possible using a limited memory Broyden–Fletcher–Goldfarb–Shanno algorithm (LBFSG) iteratively, with decreasing regularization weight. This method first optimizes the principal components for low-frequent deformations and keeps in-

creasing the frequency of deformations to optimize for high-frequency deformations. The cost function used root mean square errors. This process deforms the shape of the reference until it aligns as well as possible with the target shape. Lastly, to gain correspondence, for each point on the reference shape the closest point on the target shape is mapped. When done for all shapes, the target shapes are in correspondence with the reference and the shapes can be incorporated into the SSM [34].

3.2.7 Gaussian process regression

Now the low-rank approximation of the multivariate normal is formed over a dataset of shapes in correspondence, we can use it to predict a posterior model, using partial shapes. This posterior model shows the mean and covariance of all shapes given a certain number of observed points. This model has again the shape of a multivariate normal distribution and is called the conditional distribution. The probability of a full shape s given an observed partial shape is defined as:

$$p\left(s \mid s_g\right) s_g = N\left(\mu_c, \Sigma_c\right) \tag{3.17}$$

Were μ_c and σ_c are the conditional mean and covariance matrices. Written out this results in [33]:

$$\mu_c = \mu + Q\left(Q_g^T Q_g + \sigma^2 I_n\right)^{-1} Q_g^T \left(s_g - \mu_g\right) \tag{3.18}$$

and:

$$\Sigma_c = \sigma^2 Q\left(Q_g^T Q_g + \sigma^2 I_n\right)^{-1} Q^T \tag{3.19}$$

Where μ is the mean shape, Q contains the principal components of the prior model, Q_g contains the principal components of the observed points, μ_g is themean of observed points, σ^2 is the variance of the noise of the observations and I_n is an identity matrix.

To save computer memory, we describe the conditional shape as principal components:

$$s_c(\alpha) = \mu_c + Q_c \alpha \tag{3.20}$$

Because $Q = UD$ we can rewrite equation 3.19 as:

$$\Sigma_c = U\sigma^2 D\left(Q_g^T Q_g + \sigma^2 I_n\right)^{-1} DU^T \tag{3.21}$$

Now we can do a singular value decomposition on the middle part of the equation:11

$$\sigma^2 D\left(Q_g^T Q_g + \sigma^2 I_n\right)^{-1} D =: U_i D_i^2 U_i^T \tag{3.22}$$

yielding:

$$\Sigma_c = UU_i D_i^2 U_i^T U^T \tag{3.23}$$

Where U_i and D_i are the eigenfunctions and eigenvalues of the middle part of the equation3.21.

This can then be written as:

$$\Sigma_c = (UU_i)\, D_i^2\, (U_i U)^T \tag{3.24}$$

Note that this has the same form as equation3.16. Therefore, all variances can be expressed according to [33]:

$$Q_c = (UU_i)\, D_i \tag{3.25}$$

Now, we can express the principal components of $s_c(\alpha)$ as a function of the eigenvalues of the prior model, the principal components are contained in Equation 23. The posterior model is now expressed as the total formula for the total conditional shape s_c, given a partial shape s_g:

$$\begin{aligned} s_c(\alpha) = \mu + Q \left(Q_g^T Q_g + \sigma^2 I_n\right)^{-1} Q_g^T \left(s_g - \mu_g\right) \\ + (UU_i)\, D_i \end{aligned} \tag{3.26}$$

By doing so, the conditional shape is described as a function of the low-rank prior model and the low-rank model of the given partial shape. With this formula, the shape of a full radius can be predicted based on the given SSM and a partial shape. In our application, the full shape of a radius can be predicted given a low-rank statistical shape model of a dataset of radii, and a partial shape of a proximal radius. Because both are available, the only unknown term in the formula is the noise term σ^2. This is chosen to be 5 mm. This makes the model more general and also makes the model more robust. Additionally, an extra diagonal Gaussian kernel with a standard deviation of 200 mm was added to the model. This adds some extra low-frequency variation to the model which compensates low frequencies that are not present in our dataset. Now, all terms in equation 3.26 are known and a conditional radius can be predicted based on a partial shape.

3.3 Results

To show what variation is prominently present in the radius over our dataset the first five components of the variation of the radius are displayed at ± 2 the standard deviation.

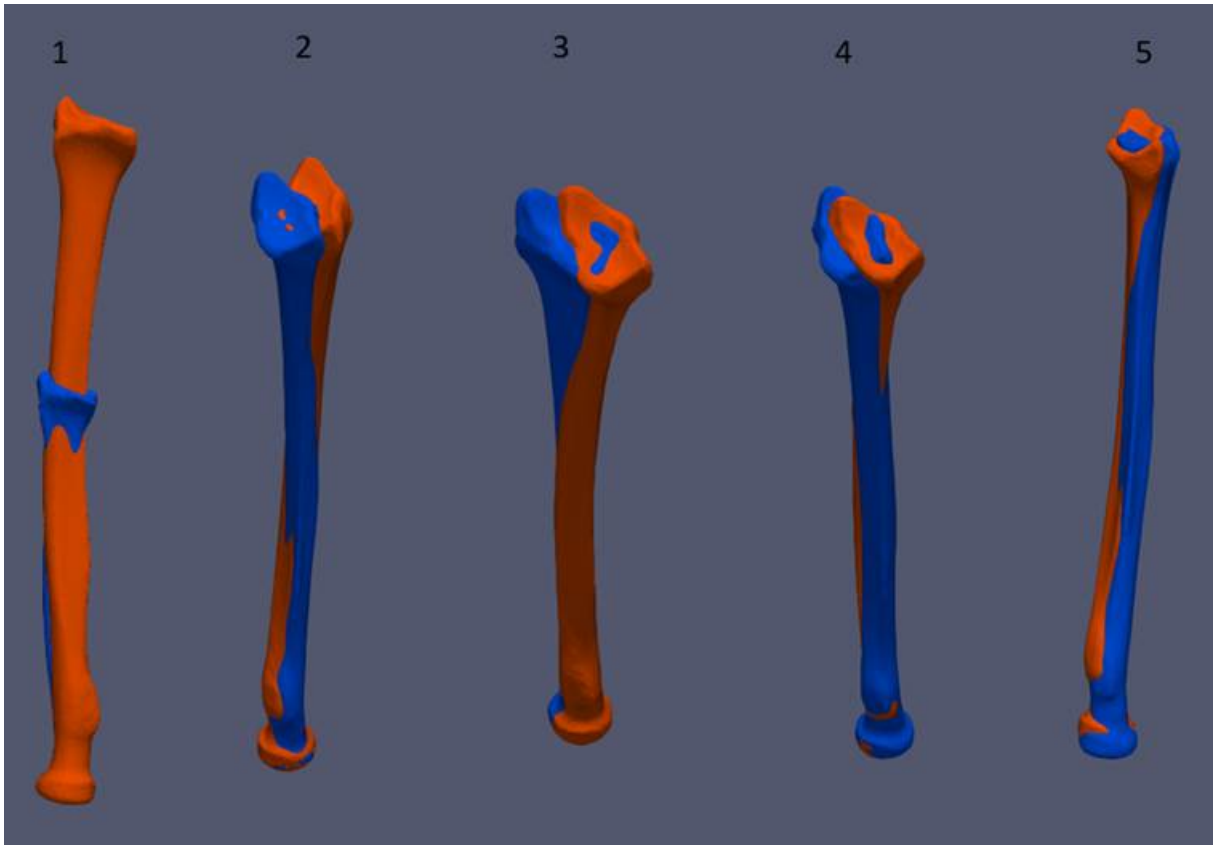

Figure 3.2: The first five principal components of the statistical shape model visualize the five main ways the shape of the radius varies (numbered from left to right). The blue and orange colors indicate the boundaries ($\pm$ 3 sd) between which most variations occur. For example, component one describes the variation in scaling in our dataset.

Figure 2 shows the five principal components. inspection suggests that the first component encodes scaling. The second component suggests a pro/supination rotation and a flexion-extension rotation. The third component suggests a pro/supination rotation even as the fourth component. The fifth component seems to show a flexing extension rotation, and also a difference in radius inclination.

To indicate how much variance each principal component covers, the eigenvalues are displayed in Figure 3 as a percentage of the total variation. Because only a rigid registration was done instead of also an affine registration scale was not excluded from the shape information. Therefore, the first component covers the scale information and covers 95 % of the variation. The other components describe just 5 percent of the total variation.

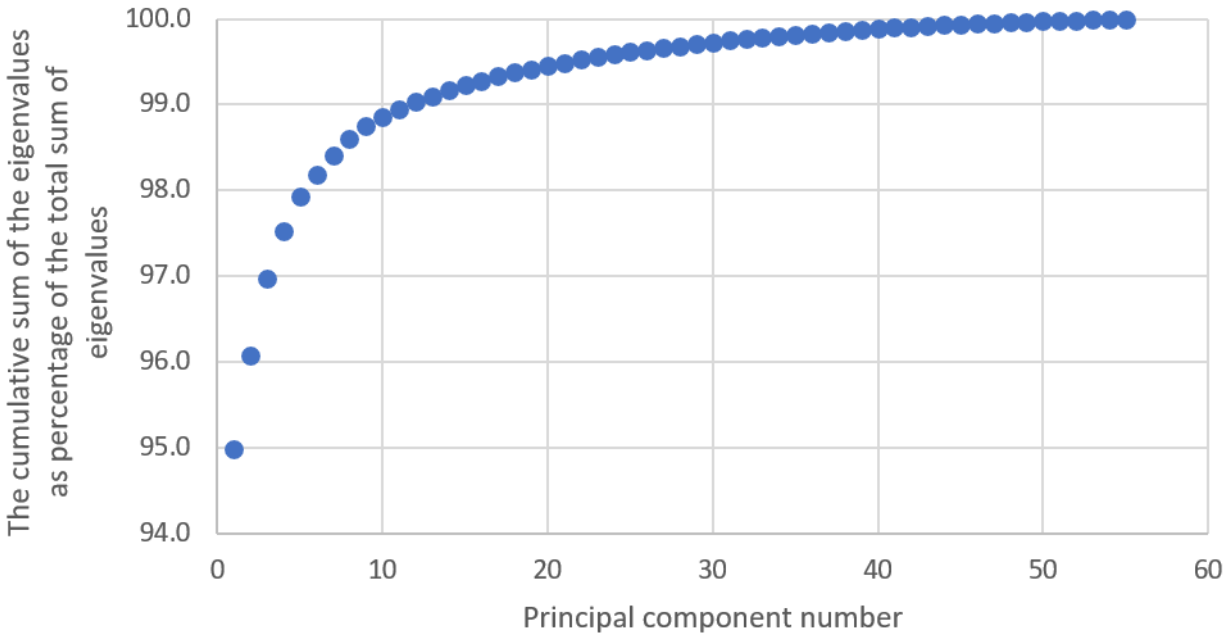

Figure 3.3: The cumulative sum of the eigenvalues of a statistical shape model of the radius, as a percentage of the total sum of eigenvalues, for all principal components. Note that the y axis starts at 94%

3.4 Discussion

By using the mathematical framework incorporated in the Scalismo coding language [35], [36], a morphable model and Gaussian process regression algorithm were successfully trained for a dataset of radii. Moreover, a visualization of the first five components suggests that most variation exists is in the scale dimension. After that, also large variations are present in ab/adduction, flexion/extension, and pro/supination rotations are present in our dataset.

The major assumption in the creation of the statistical shape model was that perfect correspondence exists between shapes. Although the method we used to establish correspondence was previously described as an accurate method, visually some errors were observed [37]. To establish correspondence, a non-rigid registration was performed. When a moving shape is morphed to a target shape, the moving shape is often stretched out or shrunk when the target shape has a larger surface in a specific area. Especially on the edges of the distal radius, some over- and under-sampling occurred. However, testing the quality of correspondence cannot be measured quantitatively. Because major landmarks are used for registration. Therefore, these areas are likely to have good correspondence. Although other landmarks can be used, they are often close to the landmarks used for registration or in

a less relevant position. The consequence of the under and oversampling induced by the establishment of correspondence is that fine details can be lost. This means that the algorithm possibly lacks the power to predict fine shape variation.

To correct for imperfect correspondence, all observed points are considered to be noisy. We added a noise term σ^2 to correct for this observation. This term was chosen to be 5 mm, which means that we assume that observations are Gaussian distributed around the real point with a variance of 5 mm. This value was not calculated analytically but based on an educated guess.

A second assumption is that all shape variation present in the dataset is covered with a finite number of principal components. However, for computational purposes, this is not possible. Especially in large shapes with large frequency deformations present, fine details can get lost because of the use of finite components. However, although the first components cover large variations, the last components cover almost no variation. This means that enough components are used and the low-rank approximation is viable.

A third design choice was that we aligned all shapes proximally. A more common approach would be to use surface registration. When doing so, the center of variation would be more in the center of the bone. For example, the first component now scales the radius with a center in the proximal radius whereas if surface registration would have been used, the scaling center would have been in the center of the bone. Because we are especially interested in the shape variation of the distal radius with a fixed coordinate system in the proximal radius, our registration approach is more insightful to display. Further, no principal components have to be used to describe translational or rotational differences in registration. However, since enough principal components are available, this would not have been a major issue in the shape prediction algorithm. Further, it is also common to use an affine registration instead of a rigid registration, since the scale is often not considered to be part of the shape. However, for our clinical application, it is insightful to consider scale as part of the shape because corrections in distal radius osteotomy happen in rotations of the distal fragment and in a length correction.

In conclusion, we were able to use the mathematical framework with the Scalismo language to create an SSM and a shape completion algorithm to predict the shape of the distal radius for distal radius correction osteotomy. The accuracy of this model has yet to be proven.

Chapter 4

Validation of a distal radius shape completion model

4.1 Introduction

A frequent complication after distal radius fractures is a malunion in which the radius heals in a non-anatomical orientation [5]–[9]. Symptoms of a distal radius malunion include pain, loss of function, wrist instability, and osteoarthritis [10]. At first, a malunion is treated conservatively. However, if complaints remain, a correction osteotomy can be considered to reconstruct the original shape of the radius [12]–[15].

To reconstruct the radius accurately, three-dimensional (3D) planning is used to see what corrections are necessary. Here, 3D computer models of the affected and contralateral forearm are generated based on computed tomography (CT). The model of the contralateral side is subsequently mirrored and superimposed on that of the affected forearm. The differences between the models of the (un-)affected forearm are assumed to be equal to the corrections that need to be obtained through the correction osteotomy. By doing so, the contralateral radius is used as a template for the correction of osteotomy [12]–[15].

The use of the contralateral forearm as a template for the correction osteotomies has several disadvantages. First, the contralateral forearm must be a correct representation of the pre-fracture forearm. Several studies, however, have shown that bilateral forearm asymmetry can be present [20], [30]. Furthermore, any bony pathology (i.e., previous trauma, congenital disease, or metabolic disease) in the contralateral radius discards the use of this radius as a template [21]. Lastly, additional radiation exposure is necessary to obtain models of the contralateral forearm. All in all, an alternative for the contralateral forearm as a template for correction osteotomies is desired.

Several authors have already reported a solution to replace the contralateral side with a different template [21], [22]. Mauler et al. and Oura et al. used statistical shape modeling to predict the shape of the distal radius based on the healthy part of the malunited radius [21], [22]. These authors demonstrated global rotational and translational differences between the predicted and original radii. Their results appeared to be comparable with the differences between the contralateral forearm and the original radius.

Not all limitations and details about the use of a predicted radius as a template for osteotomies are yet known. Except for the global rotational and translational differences between the predicted and original radius, not much is known about the local predictive performance of statistical shape models for this application. Since the main objective of distal radius osteotomies is to restore a congruent distal radioulnar (DRU) and radiocarpal joint, it is necessary to create an accurate template to reconstruct these areas [24]. If we want to use a predicted radius as a template, we need to know what regions can be predicted reliably and can therefore be used as a template and what regions are predicted less reliably and should therefore not be used as a template for osteotomy. Further, it is thought that the position of the malunion affects the performance of the algorithm [21], [22]. If the malunion is located relatively proximal, a large part of the radius must be predicted and less information about the distal shape is available and vice versa. Therefore, to use a predicted forearm as a template for osteotomy, more information is needed about local predictive performance and the impact of malunion position.

We developed a shape completion algorithm that can predict the distal radius based on the proximal part and shaft of the radius. The aim of this study was to evaluate the performance of this algorithm and to further evaluate the benefits and limits of the use of statistical shape models to predict the distal radius for correction osteotomies. This study focuses on local differences between a predicted radius and an original radius and evaluates the effect of malunion position.

4.2 Methods

4.2.1 Patients and data

In this study, 57 subjects were retrospectively included to train and evaluate a shape completion algorithm as was described in chapter 3. All subjects were patients from the ‘Orthopedisch Centrum Oost Nederland’ (OCON) and were suspected of a distal

radius malunion. Inclusion criteria were a bilateral CT scan of the whole forearm and age of $>$18 years. Exclusion criteria were a previous pathology in one of the radii other than the malunion. Inclusion occurred between February 2015 and June 2021.

CT- scan settings were based on a standard forearm scanning protocol and were obtained before the corrective osteotomy. A slice thickness between 0.2 and 0.6 mm was used, with a B20 kernel and a matrix of 512x512. The voltage used was 120 kV and the tube current was automatically regulated. The forearms were placed in the scanning direction. Segmentation was done using the protocol in appendix A.

4.2.2 Statistical shape and shape completion model

The prediction of the distal part of the radius is based on the proximal part of the radius and was done using an in-house made Gaussian process regression shape completion algorithm. This method uses the statistical shape models described in chapter 3. In short, the 3D computer models with point correspondence of all healthy radii were incorporated into a statistical shape model. This model contains the mean shape and anatomical variations present in our dataset. The variation in shape is expressed as principal components. Because the model also contains correlations between points, a shape can be predicted given a set of observed points. By doing so, the shape of the distal radius can be predicted using the shape completion algorithm and the proximal part of the radius as input.

4.2.3 Analysis

To evaluate the performance of the shape completion algorithm, a leave-one-out analysis was performed. Each healthy radius was clipped at 10% of its length. This is the point closest to where the distal radius converges to the shaft. This cutoff length is chosen because distal radius fractures happen most frequently distal to this area. When clipped, the model is trained on all data except for the clipped radius. Further, the clipped radius is used as input for the shape completion algorithm. This process is repeated for each healthy radius.

The coordinate system used for measurements is similar to that of Vroemen et al [20]. The z-axis is a line between the midpoint of the radius and the center of the articular surface, the x-axis is a line between the center of the ulnar notch and the y-axis is perpendicular to the x- and z-axes. The center of the coordinate system is in the center of the radius, which is visualized in Figure 1. A summary of the different analysis steps is visualized in Figure 2 [20].

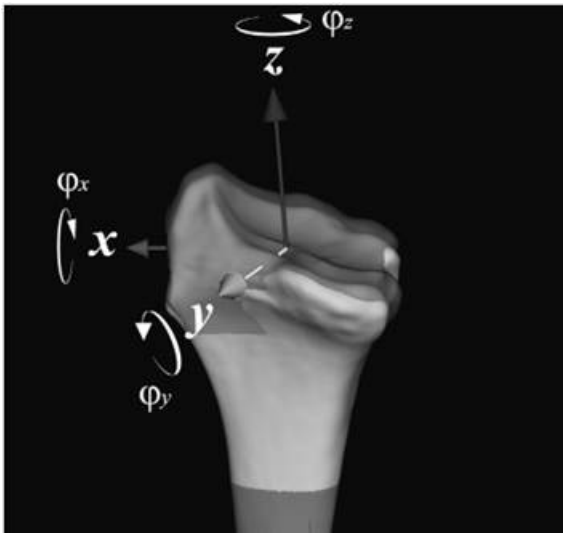

Figure 4.1: T
he anatomical coordinate system, where the z-axis is the longitudinal axis, the x-axis is toward the radial styloid, and the y-axis is perpendicular. Image adapted from Vroemen et al.

4.2.4 Quantitative evaluation

Several parameters are used to describe the difference between the predicted and original radius. First, the average point-to-surface distance and the Hausdorff distance between the predicted distal radius and the original ground-truth distal radius are calculated for each predicted radius. These results are visualized in a violin plot and the mean and standard deviation of these metrics are provided.

To show the rotational and translational differences that exist between the predicted and original radius, the predicted distal radius is aligned with the original distal radius. In this manual alignment, the articular surfaces of DRU and the radiocarpal joint are aligned as well as possible. The rotational and rotational differences are calculated as a 4x4 transformation matrix. The mean and standard deviation of the translational differences are calculated from this matrix directly. Rotations are provided as a 3D rotation and as a rotation around the x-, y-, and z-axes. The 3D rotation is defined as the angle from the axis-angle representation of the rotation matrix. The rotations around the x-, y-, and z-axes are calculated as the relative contribution of the axis-angle rotations. In this method, the angle around the x-axis is defined as the x-component of the normalized rotation axis, multiplied by the 3D angle. The same method was done for the y- and z-axes. This results in an unambiguous representation of the rotation matrix in angles around the x-, y-, and z-axes.

Another way to demonstrate how the predicted distal radius differs from its orig-

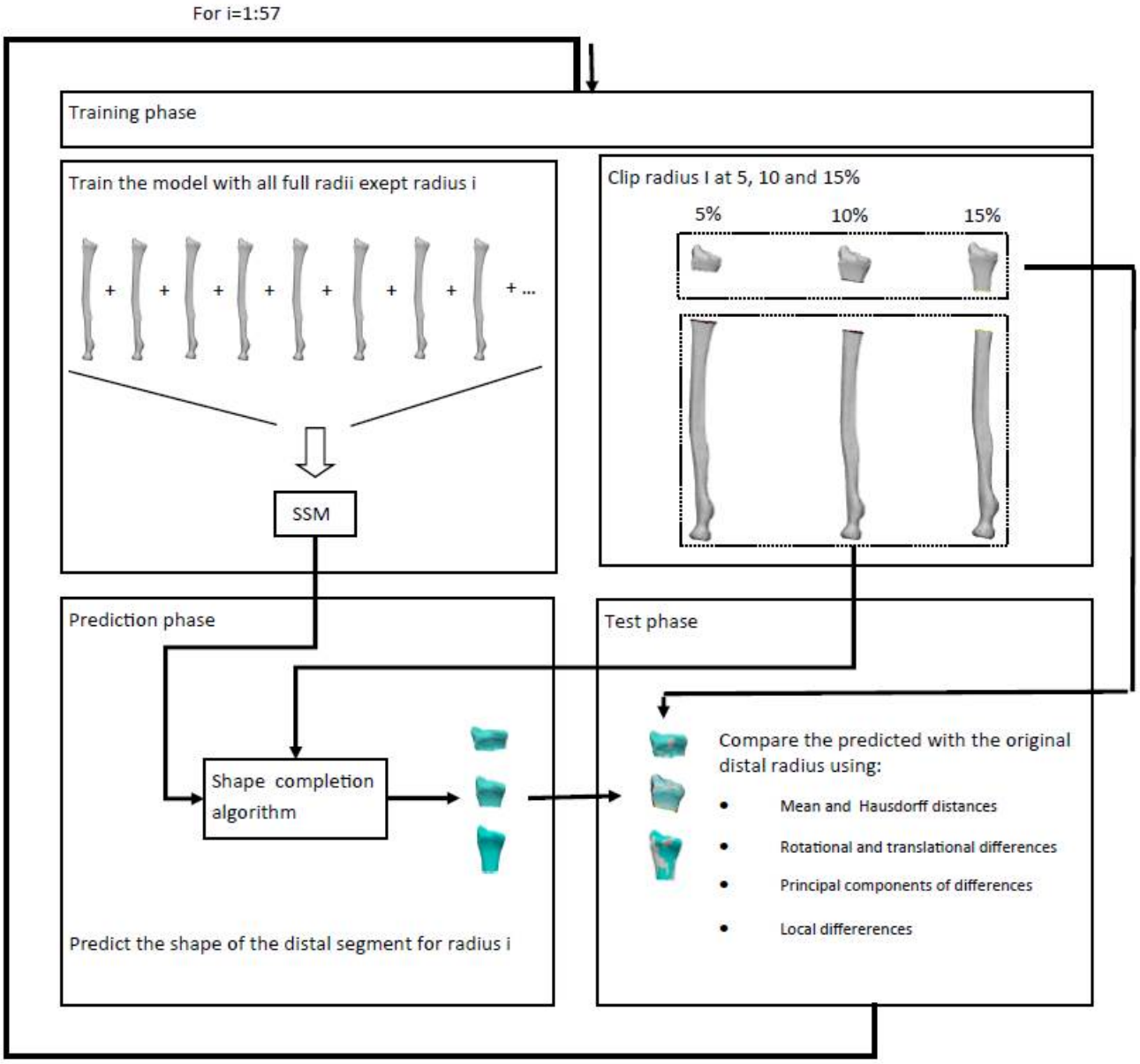

Figure 4.2: A flowchart summarizing the method. For each radius, a leave one out procedure was done in which a statistical shape model is trained, and a radius is clipped at 5%, 10%, and 15% length. Then the proximal radius is used to predict the distal radius using a shape completion algorithm. Lastly, the predicted radius is compared with the original radius.

inal counterpart is to show the principal components of the variation in differences between the predicted and original distal radii. The first 5 components are visualized at two times the standard deviation. This shows the five main ways the predicted radius differs from the original radius. The procedure to make these principal components is similar to the method described in Chapter 3. In this chapter the principal components were made from deformation vectors, these principal components are made with point-to-surface vectors.

The local differences between the original and predicted radius are visually demonstrated. Images with the mean and maximal point-to-surface differences are created to illustrate the local differences.

4.2.5 Effect of malunion position

The effect of malunion position on the performance of the shape completion algorithm is analyzed by repeating the same experiments for a setup where the distal 5% and 15% of the radius hat to be predicted. The average point-to-surface and the maximal differences between shapes (Hausdorff distances) are shown in violin plots and the mean and standard deviations are provided. The effect of malunion position on local differences is displayed by also showing the local mean and maximal differences for the distal 5% and 15% prediction setups. To show whether there is a statistical difference between the 5% and 10% predicted radius, and the 15% and 10% predicted radius, a two-tailed paired t-test was performed.

4.2.6 Size of the training set

To show whether the model is fully trained, the algorithm was also tested with low data models. we trained the model with 3 up to 56 samples. For all 53 low data statistical shape models, a leave one out analysis was performed to analyze its performances. The performance was quantified with the mean point-to-surface differences between the predicted and original shapes. This will show how the addition of more data will improve the performance of the algorithm.

4.3 Results

The average and standard deviation of the mean and Hausdorff distances for 5%, 10%, and 15% malunion segments are displayed in table 1. Its shows that there are statistically significant differences between the performance of the algorithm when predicting 5% and 15% compared to the performance when predicting 10%. No

Table 4.1: The performance of the shape completion algorithm, expressed as the average and standard deviation of the mean and Hausdorff distances between the predicted and original radius, for 5%, 10%, and 15% predicted radii

	Mean $\pm$ std (mm)	p-value	Hausdorff distance $\pm$ std (mm)	p-value
5%	0.79 $\pm$ 0.22	0.005	3.00 $\pm$ 0.69	0.086
10%	0.83 $\pm$ 0.24		3.11 $\pm$ 0.84	
15%	0.93 $\pm$ 0.33	$<$0.000	3.49 $\pm$ 1.11	$<$0.000

Table 4.2: The mean and standard deviation of the rotational and translational differences between the predicted and original radius

	Mean rotational and translational differences $\pm$ std			
	x (deg/mm)	y (deg/mm)	z (deg/mm)	3D (deg)
Difference in rotation around the axis	0.19 $\pm$ 2.64	0.15 $\pm$ 2.49	0.07 $\pm$ 3.91	4.75 $\pm$ 2.36
Difference in a translation over the axis	0.33 $\pm$ 4.74	-0.23 $\pm$ 4.72	0.31 $\pm$ 0.88	

statistical differences were found between the Hausdorff distances for 5% and 15% predicted radius. The mean and Hausdorff point-to-surface distances between every predicted and original radius are displayed for all shapes and are shown in Figures 3 and 4. This shows that the larger the predicted part of the radius is, the less accurate it can be predicted. Rotational and translational differences between the predicted and original distal radii and the mean and standard deviation are expressed in table 2.

Figure 5 shows the first 5 principal components (within two times the standard deviation) that describe the main differences between the 10% predicted radius and the original radius. Visual inspection suggests that the first component predominantly stands for ulnar/radial deviations. The second component encodes a flexion/extension rotation. The third component seems to display a combination of ulnar/radial deviation and flexion/extension. The fourth component stands for pro-/supination. The fifth and final component suggests a difference in length between the predicted and original radius.

The mean local differences between the predicted and original radius for 5%, 10%, and 15% malunion segments are shown in Figure 6. This figure shows that more local differences exist when a larger percentage of the distal radius has to be predicted. One can see that in most areas, the differences, on average, are around one millimeter. Most differences exist around the dorsal side of the radius, especially on the radial styloid and the dorsal tubercle. On the ventral side, most differences

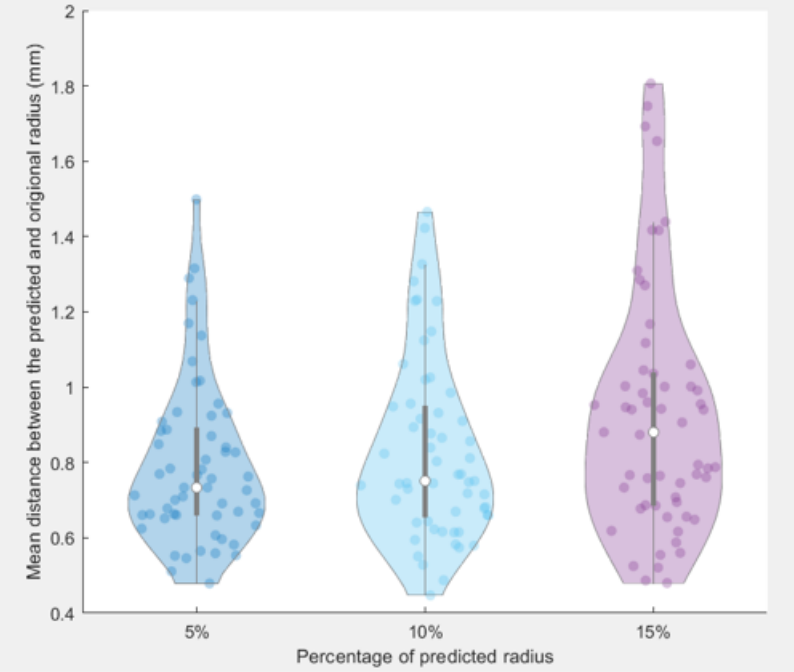

Figure 4.3: Violin plots for the mean point to surface distances between each pair of predicted and original radius for scenarios where 5%, 10%, and 15% of the radius were predicted.

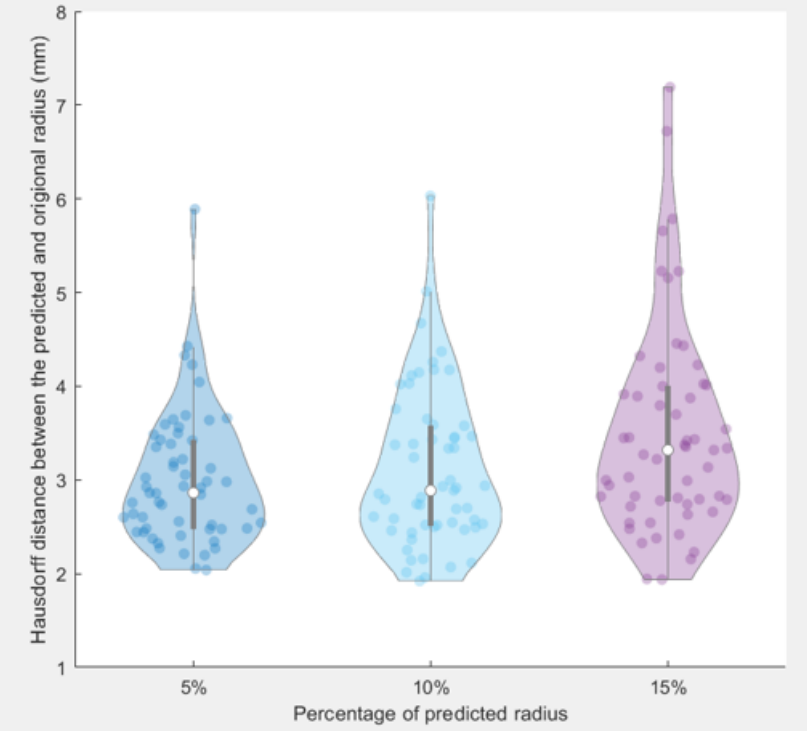

Figure 4.4: Violin plots for the Hausdorff distances between each pair of predicted and original radius for scenarios where 5%, 10%, and 15% of the radius were predicted.

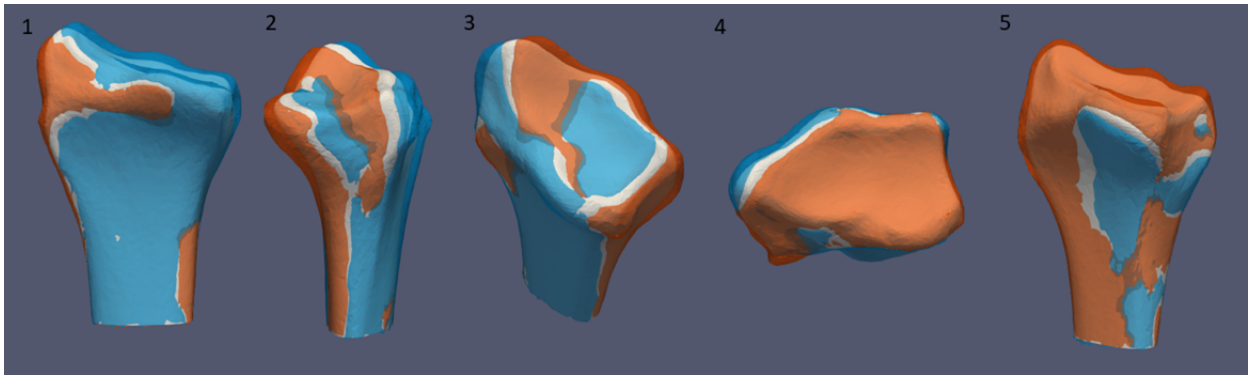

Figure 4.5: The first five principal components visualize the main differences between the predicted and original radius (numbered from left to right). An average radius is visualized in white. The blue and orange colors indicate the boundaries (±2 sd) between which most variations between the predicted and original radii occur. For example, component one suggests that most variation is present in n in rotation in radial inclination, visualized as the orientation between the orange and blue radii.

exist in the ventrodistal corner of DRU.

Figure 7 shows the maximal local differences between the predicted and original radius for 5%, 10%, and 15% malunion length. Here we see that the differences can be as large as 6.7 mm. However, these differences only occur at the radial side of the radial styloid and when 15% of the radius had to be predicted. In general, the maximal differences are below 4 mm. The keystone area and radial styloid are areas with the largest maximal difference.

Figure 8 shows the improvement of the prediction model with the addition of more training data. At first, more data improves the algorithm, but when with fifty-six samples in the training dataset, the algorithm does not improve much with the addition of extra data.

4.4 Discussion

This study shows that a statistical shape model can accurately predict the shape of the distal radius when provided with the proximal radius as input. When the shape completion algorithm has to predict a larger part of the distal radius, the accuracy of the algorithm declines. Both on a global as well as a local level, differences between the predicted and original distal radius are typically around the millimeter. Our results show that relatively few differences are present between the predicted and the original DRU and radiocarpal surfaces. This means that these areas can be used as templates for osteotomy. However, the dorsal side of the radial styloid, the dorsal

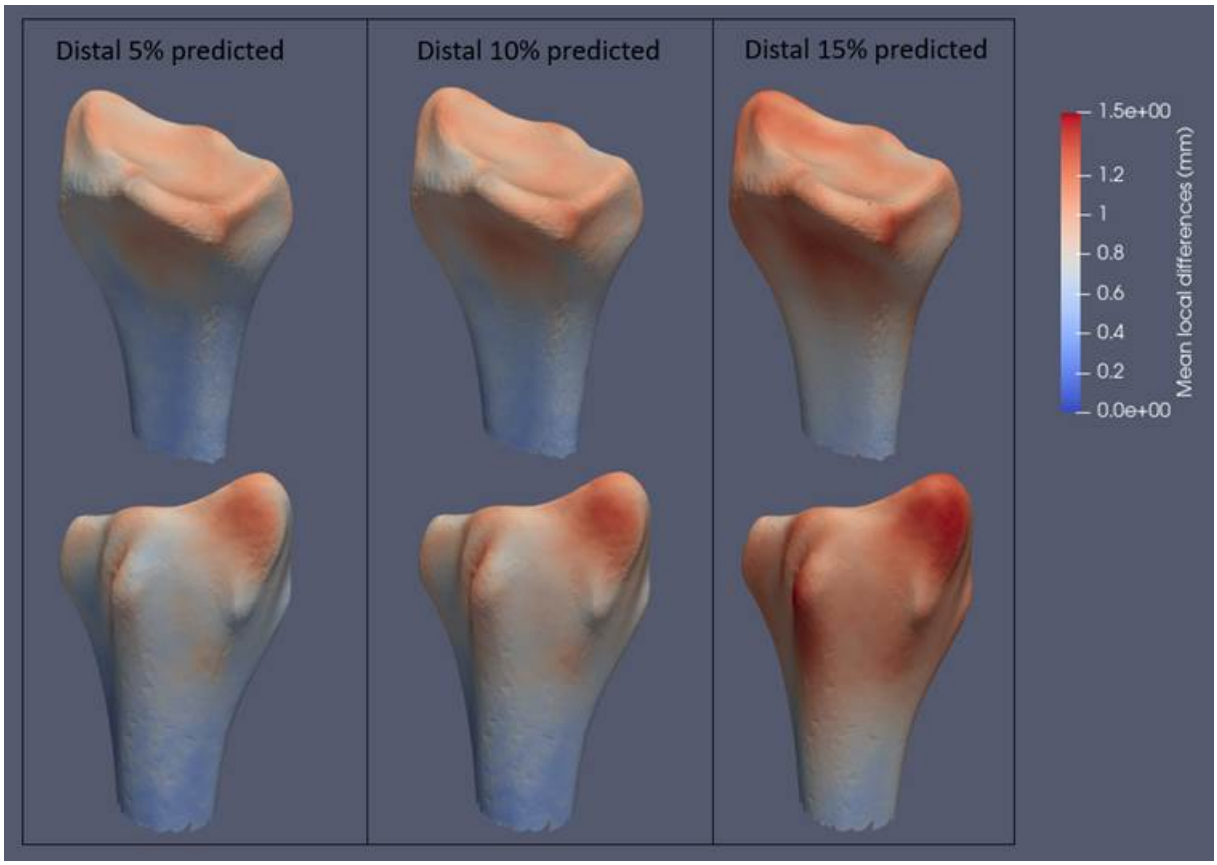

Figure 4.6: The mean local differences between the predicted and original radius, for scenarios where 5%, 10%, and 15% of the radius is predicted. Red areas contain large differences between the predicted and original radius and blue areas contain little differences.

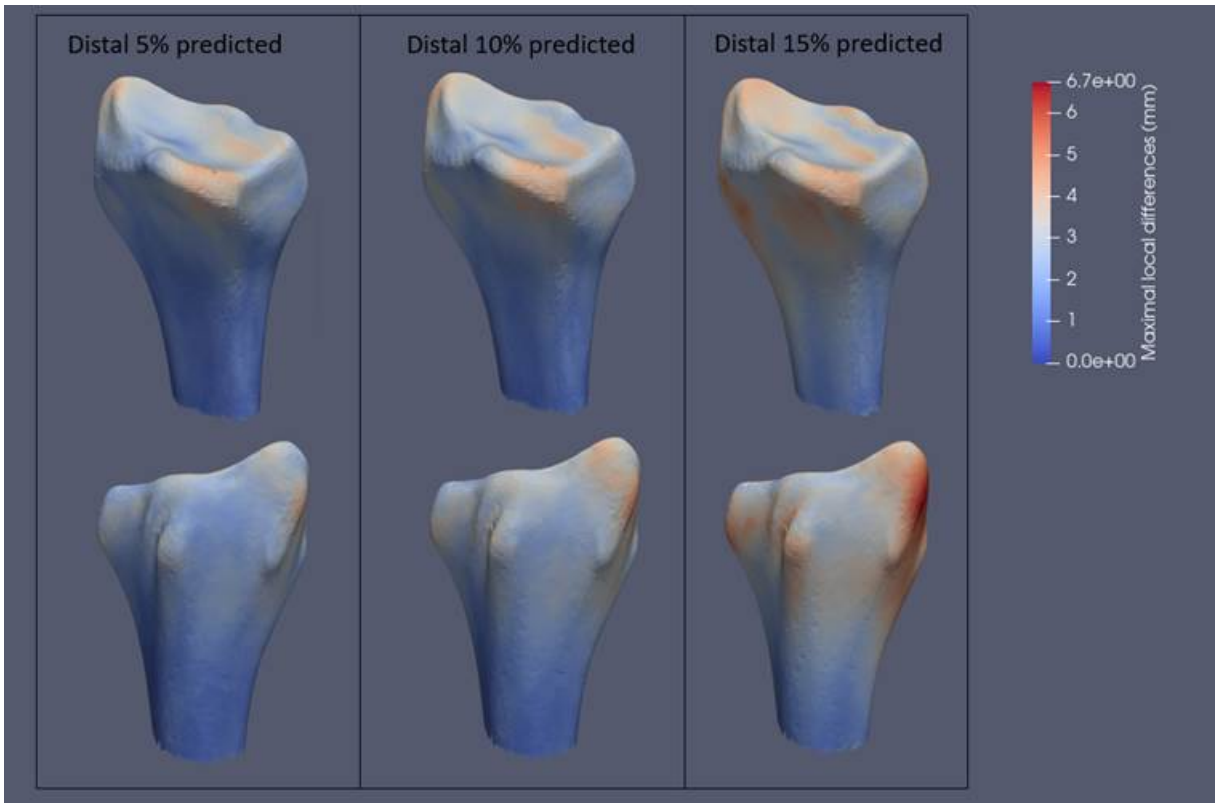

Figure 4.7: The maximal local differences between the predicted and original radius, for scenarios where 5%, 10%, and 15% of the radius is predicted. Red areas contain large differences between the predicted and original radius and blue areas contain little differences

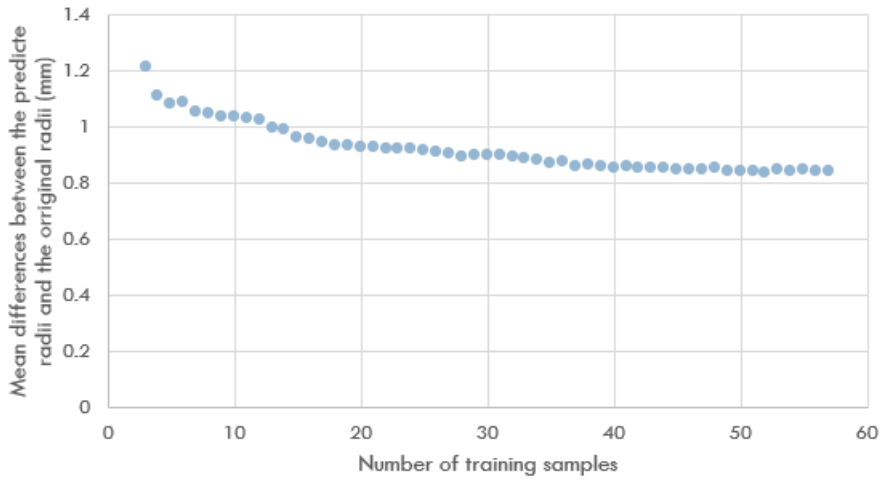

Figure 4.8: The performance of the shape completion algorithm with fewer training samples available. The performance of the algorithm is expressed in mean differences between the predicted radii and the original radii.

tubercle, and the most ventrodistal corner of DRU is predicted less accurate and should therefore preferably not be used as a template for distal radius osteotomy. Further, the rotations and translations, and the first five principal components of the variation in the difference between the predicted and the original radius show only small differences. This confirms the suggestion that small differences between the predicted and original radius exist, but the predicted radius is more or less similar to the original radius.

Our results show that if the malunion is positioned relatively proximal and the part of the distal radius that has to be predicted is therefore large, the shape completion algorithm is less accurate. This happens because less data is available and the data that is available contains less information about the distal radius. When only a small part of the distal radius has to be predicted, the performance of the model increases. This means that an as large as possible area of the radius must be used as input for the shape completion algorithm.

Further, our study shows that local differences between the predicted and original radius are primarily present on the dorsal side of the radius, especially in the radial styloid and the dorsal tubercle. An explanation could be that the shaft and proximal radius do not contain enough information about these areas to correctly predict their shape. Besides, areas with large anatomical variance are relatively hard to predict. The dorsal tubercle is known to have a considerable amount of anatomical variance [38], [39]. This may explain the relatively large errors in this region.

Previous studies investigated the use of statistical shape models to predict the shape of the radius [21], [22]. Mauler et al. used a similar statistical shape model design as the model presented here [21]. The authors used a setup where they predicted the distal 50% of the radius based on the proximal 50%. The authors found a mean point-to-surface distance of 0.71 +-0.10 mm and an average Hausdorff distance of 3.34 +-1.18 mm which is slightly better than our algorithm [21]. Oura et al. used a partial least squares regression to predict 30% of the distal radius based on 60 of the proximal radius. With a mean surface distance of 0.93 +-0.39 mm, their model performs comparably to our model [22]. However, the results are not directly comparable because the authors also predicted a larger part of the radius. Further, it is unclear how the studies by Mauler et al. and Oura et al. calculated the rotational differences between the predicted and original radius which complicates comparisons [21], [22]. One could hypothesize that the differences in the number of training samples could explain the differences since Oura et al. and Mauler et al.

used larger datasets [21], [22]. However, our results suggest that the results are not expected to improve much with the addition of more data. Our algorithm seems to perform similar to previous attempts to predict the distal radius, however, no accurate comparison can be made because of differences in design.

This study has several weaknesses. At first, the performance of the algorithm is tested with a leave-one-out method because of the limited size of our dataset. Therefore, the algorithm was made with knowledge about the dataset. This means that bias can be present and external validation is necessary. Further, the rotational and translational differences are based on a 4x4 transformation matrix which includes a translation vector and a rotation vector. Rotations around the x, y, and z-axis are derived from the rotation matrix with a method not described in the literature. A more common approach would be to use Euler angles. However, these results would be highly order-dependent. Our approach is independent of order and we think it gives a good indication of the differences in rotation. Furthermore, the translation vector from the transformation vector is also given. Because the translation is done after rotation, this vector is expected to be larger than when the translational difference would be calculated without correction for rotation. Moreover, the performance of the shape completion algorithm is tested with a leave-one-out method because of the limited size of our dataset. This means that we had to take the limitations of the dataset into account when creating the shape completion algorithm. This means that bias can be present and external validation is necessary. To assess the external validity of the model, an external dataset should be used.

In conclusion, this study shows that a Gaussian process regression shape completion algorithm can be used to create an accurate representation of a pre-fracture distal radius, based on the proximal part and shaft of the radius. The predicted radius can be used as a template for distal radius osteotomies, especially if the malunion is located above the shaft of the distal radius. Further, we have shown that especially the articular surfaces of DRU and the radiocarpal joint can be accurately predicted and can be used to plan an osteotomy. The dorsal side and the radial styloid are predicted less accurately and might therefore be less suitable to plan osteotomies. Further research should focus on a direct comparison between the use of a predicted and a contralateral radius as a template for osteotomy to further investigate the performance of the algorithm.

Chapter 5

General discussion

This study aimed to improve the understanding of both the use of the contralateral radius and a predicted radius as a template for distal radius correction osteotomy. In Chapter 2, we aimed to estimate the length differences in the forearm. We did this by comparing the differences between the left and right ulna in a dataset of 50 subjects. We found substantial length differences between the left and right forearm. Therefore, we conclude that the contralateral radius can not be used as a template for distal radius osteotomy without a length correction. In Chapter 3, we developed a statistical shape model and an algorithm that can predict the shape of a distal radius based on the proximal radius and the shaft, and in chapter 4 we validated the shape completion algorithm. The algorithm can predict the shape of the distal radius well and this prediction can be used as a template for correction osteotomy if no contralateral radius is present.

In preoperative planning for a distal radius osteotomy, an accurate reference radius is needed. Since the correction of the length of the radius is most important, the reference radius must provide a template to correct the length accurately. Both the contralateral radius with a correction for length, and the predicted radius can provide an accurate template for osteotomy. However, it remains unclear what would be a better template because no data is available about how well length correction based on the ulna length works. A dataset of healthy pairs of radii is needed to compare the performance of the predicted radii to that of the contralateral radius with length correction.

The success of the correction osteotomy is not only dependent on the quality of the reference radius, but also on the accuracy of this reference radius can be mimicked. If we can provide a very accurate reference radius, but the accuracy of surgery with patient-specific guides is low, correction osteotomy will still fail. Therefore, the accuracy of the reference radius does not have to be much better than the

accuracy of guided surgery. Further, In the main lines of this thesis, we focused on the length differences between the affected radius and the reference radius. It is clear that the length must be corrected accurately since an ulnar variance of 2 mm can already cause complaints. This is less clear for other differences in the pose of the distal radius. Therefore, it is unclear how the accuracy of the reference radius must not be the limiting factor in correction osteotomy. This means that we can not state that the quality of the reference radius is good enough for correction osteotomy.

In conclusion, this study shows for patients with a distal radius malunion that a length correction must be applied based on the ulna when the contralateral forearm is used to plan a distal radius correction osteotomy. When doing so, the radius can be restored to a state more similar to its original state. For patients with a malunion but without a contralateral radius available, this study demonstrates that a predicted radius can be used to develop patient-specific guides to reconstruct the radius more accurately. If the radius is reconstructed more accurately this may lead to fewer post-osteotomy complications and possibly fewer re-interventions.

Bibliography

[1] A. Bentohami, J. Bosma, G. J. Akkersdijk, B. Van Dijkman, J. C. Goslings, and N. W. Schep, "Incidence and characteristics of distal radial fractures in an urban population in The Netherlands," in *European Journal of Trauma and Emergency Surgery*, vol. 40, no. 3. Springer Berlin Heidelberg, 3 2014, pp. 357–361. [Online]. Available: https://link-springer-com.ezproxy2.utwente.nl/article/10.1007/s00068-014-0394-7

[2] E. Brogren, M. Petranek, and I. Atroshi, "Incidence and characteristics of distal radius fractures in a southern Swedish region," *BMC Musculoskeletal Disorders*, vol. 8, 2007. [Online]. Available: https://pubmed.ncbi.nlm.nih.gov/17540030/

[3] "Plating of the Distal Radius : JAAOS - Journal of the American Academy of Orthopaedic Surgeons." [Online]. Available: https://journals-lww-com.ezproxy2.utwente.nl/jaaos/fulltext/2005/05000/plating_of_the_distal_radius.3.aspx

[4] B. Bushnell and Bynum, "Malunion of the Distal Radius," *Journal of the American Academy of Orthopaedic Surgeons*, vol. 15, pp. 27–40, 2007. [Online]. Available: https://journals-lww-com.ezproxy2.utwente.nl/jaaos/Fulltext/2007/01000/Malunion_of_the_Distal_Radius.4.asp

[5] G. S. Athwal, R. E. Ellis, C. F. Small, and D. R. Pichora, "Computer-Assisted Distal Radius Osteotomy," *Journal of Hand Surgery*, vol. 28, no. 6, pp. 951–958, 2003. [Online]. Available: https://pubmed.ncbi.nlm.nih.gov/14642510/

[6] H. Hirahara, P. G. Neale, Y. T. Lin, W. P. Cooney, and K. N. An, "Kinematic and torque-related effects of dorsally angulated distal radius fractures and the distal radial ulnar joint," *Journal of Hand Surgery*, vol. 28, no. 4, pp. 614–621, 2003. [Online]. Available: https://pubmed.ncbi.nlm.nih.gov/12877849/

[7] K. Shea, D. L. Fernandez, J. B. Jupiter, and C. Martin, "Corrective osteotomy for malunited, volarly displaced fractures of the distal end of the radius," *Journal of Bone and Joint Surgery - Series A*, vol. 79, no. 12 79A, pp. 1816–1826, 1997. [Online]. Available: https://pubmed.ncbi.nlm.nih.gov/9409795/

[8] E. K. Shin and N. F. Jones, “Temporary fixation with the Agee-Wristjack during correctional osteotomies for malunions and nonunions of the distal radius,” *Techniques in Hand and Upper Extremity Surgery*, vol. 9, no. 1, pp. 21–28, 3 2005. [Online]. Available: https://pubmed.ncbi.nlm.nih.gov/16092815/

[9] W. p. Cooney, J. H. Dobyns, and R. L. Linscheid, “Complication of Colles’ fractures,” pp. 613–619, 1 1980.

[10] T. Graham, “Surgical Correction of Malunited Fractures of the Distal Radius,” *... : JAAOS - Journal of the American Academy of Orthopaedic Surgeons*, vol. 5, no. 5, pp. 270–281, 1997. [Online]. Available: https://journals-lww-com.ezproxy2.utwente.nl/jaaos/Fulltext/1997/09000/Surgical_Correction_of_Malunited_Fractures_of_the.5.aspx

[11] D. Ring, “Treatment of the neglected distal radius fracture,” in *Clinical Orthopaedics and Related Research*, no. 431. Lippincott Williams and Wilkins, 2005, pp. 85–92. [Online]. Available: https://journals-lww-com.ezproxy2.utwente.nl/clinorthop/Fulltext/2005/02000/Treatment_of_the_Neglected_Distal_Radius_Fracture.14.aspx

[12] S. Roner, F. Carrillo, L. Vlachopoulos, A. Schweizer, L. Nagy, and P. Fuernstahl, “Improving accuracy of opening-wedge osteotomies of distal radius using a patient-specific ramp-guide technique 11 Medical and Health Sciences 1103 Clinical Sciences,” *BMC Musculoskeletal Disorders*, vol. 19, no. 1, pp. 1–10, 10 2018. [Online]. Available: https://link-springer-com.ezproxy2.utwente.nl/articles/10.1186/s12891-018-2279-0https://link-springer-com.ezproxy2.utwente.nl/article/10.1186/s12891-018-2279-0

[13] J. G. G. Dobbe, J. C. Vroemen, S. D. Strackee, and G. J. Streekstra, “Patient-specific distal radius locking plate for fixation and accurate 3D positioning in corrective osteotomy.”

[14] M. Michielsen, A. Van Haver, V. Bertrand, M. Vanhees, and F. Verstreken, “Corrective osteotomy of distal radius malunions using three-dimensional computer simulation and patient-specific guides to achieve anatomic reduction,” pp. 1531–1535, 12 2018. [Online]. Available: https://doi.org/10.1007/s00590-018-2265-0

[15] L. Vlachopoulos, A. Schweizer, M. Graf, L. Nagy, and P. Fürnstahl, “Three-dimensional postoperative accuracy of extra-articular forearm osteotomies using CT-scan based patient-specific surgical guides Orthopedics and biomechanics,” *BMC Musculoskeletal Disorders*, vol. 16, no. 1, pp. 1–8, 11

2015. [Online]. Available: https://bmcmusculoskeletdisord.biomedcentral.com/articles/10.1186/s12891-015-0793-x

[16] J. T. Capo, K. Accousti, G. Jacob, and V. Tan, "The effect of rotational malalignment on X-rays of the wrist," *Journal of Hand Surgery: European Volume*, vol. 34, no. 2, pp. 166–172, 2009. [Online]. Available: https://pubmed.ncbi.nlm.nih.gov/19129357/

[17] J. Jensen, H. B. Tromborg, B. S. Rasmussen, O. Gerke, T. Torfing, H. Precht, and O. Graumann, "The effect of forearm rotation on radiographic measurements of the wrist: an experimental study using radiostereometric analyses on cadavers," *European Radiology Experimental*, vol. 5, no. 1, pp. 1–10, 12 2021. [Online]. Available: https://doi.org/10.1186/s41747-021-00209-1

[18] D. Ring, J. D. Patterson, S. Levitz, C. Wang, and J. B. Jupiter, "Both scanning plane and observer affect measurements of scaphoid deformity," *Journal of Hand Surgery*, vol. 30, no. 4, pp. 696–701, 7 2005. [Online]. Available: https://pubmed.ncbi.nlm.nih.gov/16039360/

[19] K. Thomason and K. L. Smith, "The reliability of measurements taken from computer-stored digitalised x-rays of acute distal radius fractures," *Journal of Hand Surgery: European Volume*, vol. 33, no. 3, pp. 369–372, 6 2008. [Online]. Available: https://pubmed.ncbi.nlm.nih.gov/18562374/

[20] J. C. Vroemen, J. G. Dobbe, R. Jonges, S. D. Strackee, and G. J. Streekstra, "Three-dimensional assessment of bilateral symmetry of the radius and ulna for planning corrective surgeries," *Journal of Hand Surgery*, vol. 37, no. 5, pp. 982–988, 5 2012.

[21] F. Mauler, C. Langguth, A. Schweizer, L. Vlachopoulos, T. Gass, M. Lüthi, and P. Fürnstahl, "Prediction of normal bone anatomy for the planning of corrective osteotomies of malunited forearm bones using a three-dimensional statistical shape model," *Journal of Orthopaedic Research*, vol. 35, no. 12, pp. 2630–2636, 12 2017. [Online]. Available: https://onlinelibrary-wiley-com.ezproxy2.utwente.nl/doi/full/10.1002/jor.23576https://onlinelibrary-wiley-com.ezproxy2.utwente.nl/doi/abs/10.1002/jor.23576https://onlinelibrary-wiley-com.ezproxy2.utwente.nl/doi/10.1002/jor.23576

[22] K. Oura, Y. Otake, A. Shigi, F. Yokota, T. Murase, and Y. Sato, "Prediction of forearm bone shape based on partial least squares regression from partial shape," *International Journal of Medical Robotics and Computer Assisted Surgery*, vol. 13, no. 3, p. e1807, 9 2017. [Online]. Available: https://doi.org/10.1002/rcs.1807

[23] N. Hollevoet and R. Verdonk, “The functional importance of malunion in distal radius fractures,” *ACTA ORTHOPAEDICA BELGICA*, vol. 69, pp. 239–245, 2003. [Online]. Available: http://hdl.handle.net/1854/LU-216736

[24] J. G. Dobbe, J. C. Vroemen, S. D. Strackee, and G. J. Streekstra, “Corrective distal radius osteotomy: Including bilateral differences in 3-D planning,” *Medical and Biological Engineering and Computing*, vol. 51, no. 7, pp. 791–797, 7 2013. [Online]. Available: https://link-springer-com.ezproxy2.utwente.nl/article/10.1007/s11517-013-1049-2

[25] J. Steele, “Handedness in past human populations: skeletal markers,” *Laterality*, vol. 5, no. 3, pp. 193–220, 7 2000. [Online]. Available: https://pubmed.ncbi.nlm.nih.gov/15513142/

[26] R. A. Lazenby, “Skeletal biology, functional asymmetry and the origins of ”Handedness”,” *Journal of theoretical biology*, vol. 218, no. 1, pp. 129–138, 2002. [Online]. Available: https://pubmed.ncbi.nlm.nih.gov/12297075/

[27] S. L. Bass, L. Saxon, R. M. Daly, C. H. Turner, A. G. Robling, E. Seeman, and S. Stuckey, “The effect of mechanical loading on the size and shape of bone in pre-, peri-, and postpubertal girls: a study in tennis players,” *Journal of bone and mineral research : the official journal of the American Society for Bone and Mineral Research*, vol. 17, no. 12, pp. 2274–2280, 12 2002. [Online]. Available: https://pubmed.ncbi.nlm.nih.gov/12469922/

[28] B. M. Auerbach and C. B. Ruff, “Limb bone bilateral asymmetry: variability and commonality among modern humans,” *Journal of Human Evolution*, vol. 50, no. 2, pp. 203–218, 2 2006.

[29] W. N. Arifin, “Introduction to sample size calculation,” *Education in medicine journal*, vol. 5, no. 2, 2013. [Online]. Available: https://eduimed.usm.my/EIMJ20130502/EIMJ20130502_12.pdf

[30] E. Hong, D. S. Kwak, and I. B. Kim, “Morphological symmetry of the radius and ulna—Can contralateral forearm bones utilize as a reliable template for the opposite side?” *PLOS ONE*, vol. 16, no. 10, p. e0258232, 10 2021. [Online]. Available: https://journals.plos.org/plosone/article?id=10.1371/journal.pone.0258232

[31] M. O. Gauci, “Patient-specific guides in orthopedic surgery,” *Orthopaedics & Traumatology: Surgery & Research*, vol. 108, no. 1, p. 103154, 2 2022.

[32] S. F. Baumbach, J. Binder, A. Synek, F. G. Mück, Y. Chevalier, E. Euler, G. Langs, and L. Fischer, "Analysis of the three-dimensional anatomical variance of the distal radius using 3D shape models," *BMC Medical Imaging*, vol. 17, no. 1, 3 2017.

[33] T. Albrecht, M. Lüthi, T. Gerig, and T. Vetter, "Posterior shape models," *Medical Image Analysis*, vol. 17, no. 8, pp. 959–973, 12 2013.

[34] M. Lüthi, T. Gerig, C. Jud, T. V. I. t. o. pattern, and u. 2017, "Gaussian process morphable models," *ieeexplore.ieee.org*. [Online]. Available: https://ieeexplore.ieee.org/abstract/document/8010438/

[35] "Statistical Shape Modelling - Online Course." [Online]. Available: https://www.futurelearn.com/courses/statistical-shape-modelling

[36] "GitHub - unibas-gravis/scalismo: Scalable Image Analysis and Shape Modelling." [Online]. Available: https://github.com/unibas-gravis/scalismo

[37] M. Lüthi, C. Jud, T. Gerig, and T. Vetter, "Gaussian Process Morphable Models," 2016.

[38] H. Clement, W. Pichler, D. Nelson, L. Hausleitner, N. P. Tesch, and W. Grechenig, "Morphometric Analysis of Lister's Tubercle and Its Consequences on Volar Plate Fixation of Distal Radius Fractures," *Journal of Hand Surgery*, vol. 33, no. 10, pp. 1716–1719, 12 2008. [Online]. Available: http://www.jhandsurg.org/article/S0363502308006680/fulltexthttp://www.jhandsurg.org/article/S0363502308006680/abstracthttps://www.jhandsurg.org/article/S0363-5023(08)00668-0/abstract

[39] Ağır, M. N. Aytekin, F. Küçükdurmaz, S. Gökhan, and U. Y. Çavuş, "Anatomical Localization of Lister's Tubercle and its Clinical and Surgical Importance," *The Open Orthopaedics Journal*, vol. 8, no. 1, pp. 74–77, 5 2014.

[40] J. Van den Broeck, E. Vereecke, R. Wirix-Speetjens, and J. Vander Sloten, "Segmentation accuracy of long bones," *Medical Engineering & Physics*, vol. 36, no. 7, pp. 949–953, 7 2014.

Appendix A

A.1 Segmentation

Both forearms were segmented to create a 3D surface model using mimics (materialize, Leuven, Belgium). The bones were first segmented with a thresholding function at 300 Hounsfield units, then the ulnae were selected with a build-in region growing algorithm. If multiple bones were selected, the split mask function was used to separate the bones. The gabs in the ulnae were filled using a hole-filling algorithm with an appropriate closing distance. With manual assistance, the remaining holes were filled. The segmentation method was previously validated and was considered to be accurate [40].